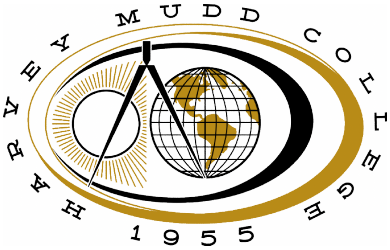

Why Higher Order Mean Motion Resonances are Weak: A Physical and Geometric Model

Elizabeth Jones

Daniel Tamayo, Advisor

May, 2025

Department of Physics

Abstract

Mean motion resonances (MMRs) play a central role in shaping orbital dynamics, both by driving chaotic behavior and by defining regions of long-term stability. In a planetary system, an MMR arises when two planets orbit a star with periods that form a ratio of integers. Specifically, in a p:$p-q$ resonance, the inner planet completes p orbits for every $p-q$ orbits of the outer planet. The traditional disturbing function expansion in celestial mechanics gives rise to MMRs whose strengths scale at small eccentricities (e) as e^q, where q is the order of the resonance. This central result makes it possible to focus on low-order p:$p-q$ MMRs and ignore the infinite number of other integer period ratios with large q corresponding to higher order MMRs. However, this relationship derived from a technical perturbation series expansion provides little physical intuition. In this thesis we instead provide a simple physical explanation for this result for closely spaced orbits. In this limit, interplanetary interactions are negligible except during close encounters at conjunction, where the planets impart a gravitational "kick" to each other's mean motion. For a qth order p:$p-q$ MMR, the inner planet completes q more orbits than the outer planet each cycle. Since a conjunction occurs each time the inner planet overtakes the outer planet, there are q conjunctions per cycle. By considering previously known Fourier expansions for the magnitude of the kick at conjunction, we show that the q-fold symmetry in conjunction locations leads to a cancellation of terms up to order e^{q-1}. Thus, we show that the weakness of high-order MMRs is due to the canceling effects of multiple conjunctions, and quantitatively explain their strength scaling as e^q. We show how this physically intuitive picture provides additional insight on the structure of additional corrections beyond the leading order behavior, and discuss its regimes of applicability.

Acknowledgements

This project would not have been the same without the people who supported me along the way. First and foremost, thank you to Professor Dan Tamayo for being an exceptional advisor—your clear explanations, thoughtful feedback, and steady support made this project both possible and deeply enjoyable. I'm also grateful for your mentorship beyond the research, from insightful discussions to sunrise hikes up Mt. Baldy with the lab group! Thanks also to Mickey Teekamongkol for being an amazing research partner last summer and helping shape the direction of this project. To my friends in the physics department: thank you for the camaraderie, the constant inspiration, and physics debates during late-night runs to L'moon. And to my family—thank you for encouraging my love of physics every day through your example and support.

Contents

Chapter 1

Introduction

1.1 Background

In our Solar System, Neptune orbits the Sun three times for every two orbits of Pluto. Such an integer ratio between a pair of orbital periods is called a mean motion resonance (MMR), so we say that Neptune and Pluto are in a 3:2 MMR. Much more than a simple coincidence, such MMRs act as a double-edged sword that in some scenarios orchestrate a stable, repeating clockwork dance, while in others they drive chaos and dynamical instabilities.

The crossing orbits of Neptune and Pluto provide an example of a stabilizing MMR. If their angular frequencies had no relationship to one another, eventually the two bodies would by chance end up at the same location at the same time and collide. However, the MMR synchronizes their motion so that the two never meet at the same place; it ensures that the faster Neptune always overtakes Pluto near the azimuthal location where the two orbits are maximally separated. As a result, the planets never risk close approaches or collisions, so here the resonance acts to stabilize the system.

On the other hand, Kirkwood gaps in the Asteroid belt illustrate the destabilizing effects of MMRs. These "gaps" of low asteroid density correspond to regions that are in a resonant period ratio with Jupiter (see Fig. 1.1). These missing asteroids are thought to have been perturbed by Jupiter to high enough eccentricities to cross the orbits of the inner terrestrial planets [22], providing a delivery mechanism for meteorites and potentially even for the K-T impact that killed the dinosaurs 65 Myr ago [1]. The absence of objects in the Kirkwood gaps illustrates that this is an unstable resonant configuration rather than a stable one. In fact, resonances are always at the heart of driving dynamical chaos in systems interacting through conservative forces [11, 12].

Ultimately, the reason why MMRs play an outsized role in orbital dynamics is the fact that they make it possible for small gravitational perturbations to repeat, so that they build up coherently and lead to large cumulative effects. In plane-

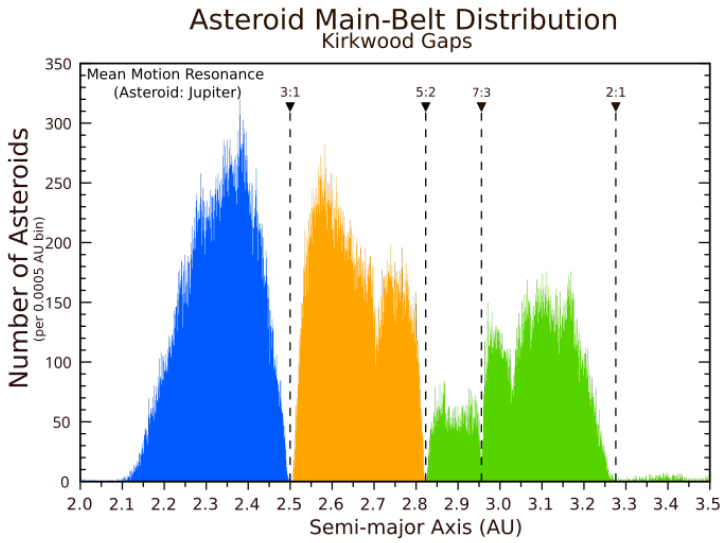

Figure 1.1: Distribution of asteroids in the main asteroid belt as a function of orbital semi-major axis, illustrating the presence of Kirkwood gaps—regions of significantly reduced asteroid density. These gaps occur at locations where an asteroid's orbital period forms a simple integer ratio (e.g., 3:1, 5:2, 7:3, 2:1) with that of Jupiter, corresponding to mean motion resonances (MMRs). Each of these MMRs corresponds to a specific semi-major axis distance (AU), marked by vertical dashed lines (recall that period P and semi-major axis a are related using Kepler's third law, where $P^2 \propto a^3$). At these locations, the MMR with Jupiter leads to chaotic orbital evolution and long-term instability, resulting in a depletion of asteroids. This demonstrates that not all MMRs are stabilizing; in some configurations, the resonance acts to destabilize orbits and evacuate the region of material. Figure adapted from an image by Alan Chamberlain [2].

tary systems, each planet's motion is primarily governed by the gravitational pull of the much more massive central star. The gravitational forces from other planets are much weaker and act as small perturbations to each orbit. Because different planets orbit at different rates, their conjunction locations—when the inner planet overtakes the outer and they pass close enough to cause a significant perturbation—are randomly distributed, causing their mutual perturbations to effectively average out. However, when two planets are in a mean motion resonance, the integer ratio of their periods causes their conjunction positions to repeat periodically. This causes otherwise small gravitational effects to build up coherently to significantly larger amplitudes. MMRs show up prominently not only in planetary orbits, but also the dynamics of moons, planetary rings, and the interactions of planets and even black holes with massive gas disks [4].

In general, an MMR occurs when two planets orbit a star with orbital periods that form an integer ratio, such as 3:2 or 5:3. But one can imagine infinitely many possible integer period ratios along the semi-major axis range on the x-axis of Fig. 1.1. Why is it that only certain MMRs, e.g., the 3:1 are prominently vacated, and not, for example, the 11:4 MMR at 2.64 AU?

The answer is a well known result in orbital mechanics: the strength of a $p:(p-q)$ MMR is proportional to e^q for low orbital eccentricities e.[1] Due to the small eccentricities in the Solar System, MMRs are much weaker for large values of q; because of this strength hierarchy, this parameter q is called the order of the resonance [8, 13]. This is why the most prominent Kirkwood gaps correspond to low-order MMRs (Fig 1.1): the 2:1 resonance—first order—truncates the outer edge of the asteroid belt, and we observe progressively smaller gaps for the second-order MMR (e.g. 3:1), third order (e.g. 5:2), and so on.

It is worth emphasizing that this hierarchy in MMR strengths is strongly tied to orbital stability. The range of semimajor axes spanned by the asteroid belt (x-axis in Fig. 1.1) is densely filled with resonances with Jupiter at arbitrary integer ratios. If they were all of comparable strength, all regions would be evacuated and there would be no asteroid belt. The hierarchy of resonance strengths is thus intimately tied to the question of which orbital configurations can persist [6], and what makes stability possible in the first place.

In the traditional orbital mechanics literature, the e^q MMR strength scaling derives from a sophisticated edifice of perturbation theory built up over hundreds of years (see Chapter 6 of [13]). The central problem is that the gravitational interaction potential Gm_1m_2/r changes in a complicated way as the planets orbit at different rates and their interplanetary separation r varies. The traditional approach exploits the periodicity of the potential in the azimuthal longitudes of the planets (if one cycles both the phases of the planets along their orbits by 2π, one is back at the same place and the potential is unchanged) to Fourier expand this interaction potential and express the Fourier amplitudes in terms of the orbital elements.[2] These Fourier amplitudes are then constant in the unperturbed problem where the orbital elements are fixed, and vary slowly in the perturbed problem since the forces between the planets are so much smaller than those from the star. In this picture, each MMR turns out to correspond to a single cosine term in this expansion. When the Fourier amplitudes are Taylor expanded in powers of the eccentricity, one finds that the Fourier amplitude, a.k.a. the "strength", of a qth-order MMR scales as e^q at leading order in the eccentricities [13].

This sophisticated traditional approach is extremely powerful and has been profitably applied in a wide range of contexts. However, it offers little physical

[1] Recall that for an elliptical orbit $0 \leq e < 1$

[2] This Fourier expansion is in terms of the so-called 'resonant angle' ϕ, which is a combination of several orbital elements, as outlined in Chapter 6 of [13]

intuition, which is problematic given the ubiquity of MMRs across various astrophysical settings and the importance of this result to how their dynamics are analyzed. This thesis offers an alternative, physically motivated explanation for this resonance hierarchy.

1.2 Outline of this Work

A main challenge is that in the general problem of two interacting planets, the gravitational accelerations they impart on one another are comparable in magnitude throughout their orbits so one has to consider their integrated effects. In this general case, the perturbative expansion of the interplanetary interaction, known as the "disturbing function," remains the most effective analytical framework available despite its considerable mathematical complexity. In this thesis, we adopt a complementary approach by focusing on the limit in which the orbits are closely spaced.

In the closely spaced limit, the interplanetary interactions are no longer comparable throughout the orbits, but instead become strongly localized to the close approaches at conjunction when the faster inner planet overtakes the outer body, and their separation is minimized [9]. The rest of the time the planets remain well separated, and their mutual gravitational influence is negligible. This allows for a simplified treatment in which the dynamics can be approximated as a discrete map: the planets follow unperturbed Keplerian orbits between conjunctions, with impulsive gravitational kicks applied at each close approach [3].

This closely spaced limit captures the dynamics of the strongest (first-order) MMRs, whose integers are separated by one, e.g. the 2:1, 3:2, 4:3 etc (see above). Since similar orbital periods with ratios close to unity correspond to close separations, the most widely spaced first-order MMR is the 2:1. Even in this widest case, the fractional spacing between the semimajor axes $\Delta a/a$ is still only ≈ 0.4. It is also applicable to higher order MMRs with period ratios $\lesssim 2$, e.g. all second-order MMRs except the 3:1, all third-order MMRs except the 4:1 and 5:2, etc. This close-spacing approximation is therefore a useful model for the majority of MMRs observed across astrophysical systems, which tend to be the strong ones.

In this thesis, Sec. 2 describes the geometry and defines the relevant variables for this 3-body system. Sec. 3 provides a qualitative description of resonance. It also takes the discrete treatement of the effects of successive conjunctions, and “smooths" it out into a continuous differential equation for how the azimuthal location of conjunction θ changes over long timescales, as a function of the gravitational effect of an individual conjunction. Sec. 4 then considers the effects of each conjunction in detail, building on work by [14], and reproducing the classical result that for a first-order MMR, the dynamics of the conjunction angle θ follows those of a simple pendulum [13]. It also provides a simple explanation for why the strength of the pendulum restoring force for a first-order

MMR scales linearly with the eccentricity, as simply the leading-order term in a Taylor-series expansion in powers of the eccentricity.

Sec. 5 lays out the novel contribution of this thesis by tackling the following paradox: if in the closely spaced limit, the interplanetary interactions are always dominated by conjunctions, and their effects to leading order scale linearly with the eccentricity, why wouldn't the strengths of all MMRs (with any integer ratio) scale linearly with e and have comparable strengths? The key insight is that in a qth order MMR, say an 11:11-q, the inner planet completes 11 orbits in the same time the outer planet completes $11-q$. If we imagine the planets racing around their respective tracks, this means that the inner planet laps the outer planet q times. In general then, for a qth order MMR, the inner planet overtakes the outer q times so there are q conjunctions per resonant cycle. In Sec. 5, we exploit the fact that the weakly perturbed planetary orbits are nearly Keplerian to first argue that the q conjunctions in a given cycle are equally separated in azimuth. We then demonstrate that this symmetry causes the effects of the various conjunctions to cancel up to order e^{q-1}. This provides a physical picture for the traditional result that the first surviving term always scales as e^q.

We lay out our conclusions and discuss other practical application of this new approach in Sec. 6. In a single sentence, higher order resonances are weak because they involve multiple conjunctions per cycle, and their effects largely cancel out. This provides physical intuition for an otherwise opaque result at the heart of orbital mechanics, which has far-reaching consequences for important questions of what types of orbital configurations can persist and be observable.

Chapter 2

Description and Geometry of the System

The argument developed in this thesis relies on a simplified model of planetary motion to isolate the essential dynamics of resonant interactions. We now turn to a more precise formulation of this model, establishing the geometric and dynamical framework in which the analysis will take place. Our goal in this chapter is to define the assumptions and coordinate systems that underlie the discrete-kick approach.

2.1 Geometry of the Circular Restricted 3 Body Problem

We consider a planetary system with two planets orbiting a central star of mass M (see Fig. 2.1). The inner planet has mass $m \ll M$ and follows a circular orbit, while the outer planet is a massless test particle on an eccentric orbit.

Given that the star is much more massive than the inner planet, we approximate the star as fixed at the center of mass of the system. Furthermore, because the outer planet is a massless test particle, it does not impart any gravitational forces on the inner planet. The inner planet therefore moves on an unperturbed circular orbit of radius a_p (red orbit in Fig. 2.1). The planet's angular position along its orbit is given by its mean longitude, λ_p, which increases at a constant rate n_p as the planet orbits the star.

Though the outer test particle technically experiences gravitational attraction from both the star and the inner planet, since $m \ll M$, these interactions are dominated by the star. The gravitational force due to the inner planet is treated as a small perturbation to this two-body problem. Therefore, to first order, the outer planet follows a Keplerian orbit with eccentricity e and semimajor axis a (blue orbit in Fig. 2.1).

The planet's angular position is given by the mean longitude λ, which corresponds to the longitude it would have if the orbit were circular. The orientation of the test particle's orbit within the orbital plane is denoted by the longitude of pericenter ϖ, which represents the angular position of the pericenter, the closest point of the orbit to the star within the orbital plane.

For simplicity, we restrict our study to two-dimensional motion and assume the planetary orbits are coplanar with orbital inclination $i = 0$.

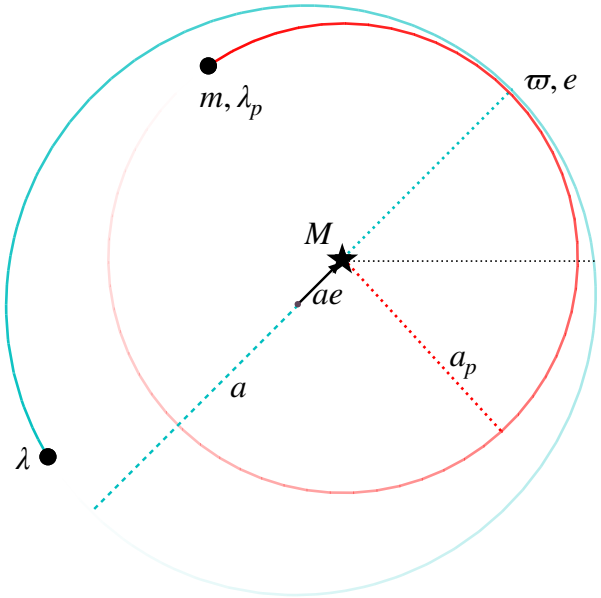

Figure 2.1: Schematic of the coplanar circular restricted three-body problem (CR3BP). A central star of mass M is orbited by an inner planet (red) of mass $m \ll M$ on a circular orbit of radius a_p and mean longitude λ_p. A massless test particle (blue) follows an eccentric Keplerian orbit with semimajor axis a, eccentricity e, and mean longitude λ. The orbit's orientation is set by the longitude of pericenter ϖ, measured from the reference angle at the horizontal dotted black line. The star is fixed at the center of mass, and the inner planet's gravity perturbs the test particle only at close approaches. For illustrative purposes, the eccentricity is exaggerated and set to the crossing value e_c, at which the orbits just begin to intersect. This geometry forms the basis for our discrete-kick model of resonant interactions.

This system is commonly referred to as the coplanar circular restricted three body problem (CR3BP). Though this simplified model may seem restrictive, it has been shown that, for closely spaced orbits, the CR3BP can be approximately

mapped onto the more general problem of two massive planets both with eccentric orbits [5]. Tamayo and Hadden (2025) offer a physical and geometric explanation for this mapping [18]. As a result, despite using the simplified CR3BP, our conclusions are equally applicable to the broader problem of two eccentric, massive planets in the closely spaced limit.

2.2 Normalized Eccentricity and Orbit Crossing

For orbits with small eccentricities, the absolute eccentricity e is often not an informative parameter for the dynamical evolution as it gives little intuition for how close two orbits are to intersecting each other. In the CR3BP, even if the test particle's eccentricity is very small, it still may intersect the inner planet's circular orbit provided they have similar semimajor axes a and a_p. Therefore, it is more useful to define a normalized eccentricity $\tilde{e}$:

$$\tilde{e} = \frac{e}{e_c} \tag{2.2.1}$$

where the crossing eccentricity e_c is the minimum eccentricity required for the two orbits to cross one another. The quantity $\tilde{e}$ provides a natural measure of how close the two orbits are to intersecting one another, independent of the absolute size of the eccentricity [6].

The value for e_c can be determined from the geometry of the CR3BP (see Fig 2.1, in which the test particle has eccentricity e_c and the two orbits just overlap). Recall that the distance from the center of an ellipse to its focus is ae, where a is the length of its semimajor axis and e is its eccentricity. Thus, the inner planet's circular orbit is offset from the center of the ellipse by a distance ae. The two orbits cross when the difference in semimajor axes $\Delta a = a - a_p$ is equal to this offset distance:

$$e_c \equiv \frac{\Delta a}{a}. \tag{2.2.2}$$

Generally, an MMR is defined in terms of the planets' period ratio $p : p - q$ rather than through the ratio of their semimajor axes, so it is convenient to rewrite Eq. 2.2.2 in terms of these variables. We can use derivatives Kepler's third law to relate the semimajor axis a and period P of an orbit: for closely spaced orbits where $\Delta a/a$ and $\Delta P/P$ are small,

$$\frac{\Delta P}{P} \approx \frac{3}{2}\frac{\Delta a}{a}. \tag{2.2.3}$$

For planets near a p:$p-q$ mean motion resonance, the test particle's period is approximately $(p-q)/p$ times the period of the inner planet, yielding

$$\Delta P \approx P\left(1 - \frac{p-q}{p}\right) = P\left(\frac{q}{p}\right). \tag{2.2.4}$$

Substituting into Eq. 2.2.2, the crossing eccentricity for for planets near a $p : p - q$ MMR is

$$e_c \equiv \frac{\Delta a}{a} \approx \frac{2}{3}\frac{\Delta P}{P} \approx \frac{2q}{3p}. \tag{2.2.5}$$

2.3 Hill Limit

Throughout this thesis we work in the compact or Hill Limit where the two orbits are closely spaced and the eccentricities are small.

In this limit, there are two small parameters:

$$\frac{\Delta a}{a} \ll 1 \quad \text{and} \quad e \ll 1, \tag{2.3.1}$$

where $\Delta a \equiv a - a_p$ is the difference in semimajor axis length between the two orbits. The first requirement ensures that the orbits are closely spaced, while the small eccentricity requirement ensures that the orbits do not cross each other.

In this limit, it is convenient to adopt a frame rotating with the inner planet's constant mean motion n_p. In the rotating frame, the inner planet remains fixed at the origin. For sufficiently small Δa, we can neglect the effects of curvature and the relative radial and angular motion of the outer planet reduces to a linear system in Cartesian coordinates [19]. The position of the outer planet relative to the inner planet in these coordinates is:

$$x = r - a_p, \tag{2.3.2}$$

$$y = a_p \theta_{\text{rel}}, \tag{2.3.3}$$

where θ_{rel} is the angle between the two planets position vectors.

For an outer test particle traveling on a circular path, its position in the rotating frame remains at fixed $x = \Delta a$. Its angular speed n is slightly less than n_p of the inner planet, so as time evolves the test particle drifts downward in a straight line in the rotating frame (i.e. downward along the dotted black line in Fig 2.2). An eccentric test particle, by contrast, exhibits additional oscillations in the radial (x) direction of amplitude $\sim ae$, as it moves between pericenter and apocenter. Thus, an eccentric test particle's motion consists of an epicyclic oscillation in the x direction in addition to a slow azimuthal (y-direction) drift relative to the planet (solid blue line). Note that the planets meet in conjunction when they share the same azimuthal angle at $y = 0$.

Following the argument from Tamayo and Hadden (2025), we consider two important timescales in the Hill limit [18]. The first is the time between successive conjunctions. We can use the difference in the mean motions to calculate the time from one conjunction to the next, i.e., the time it takes the difference in

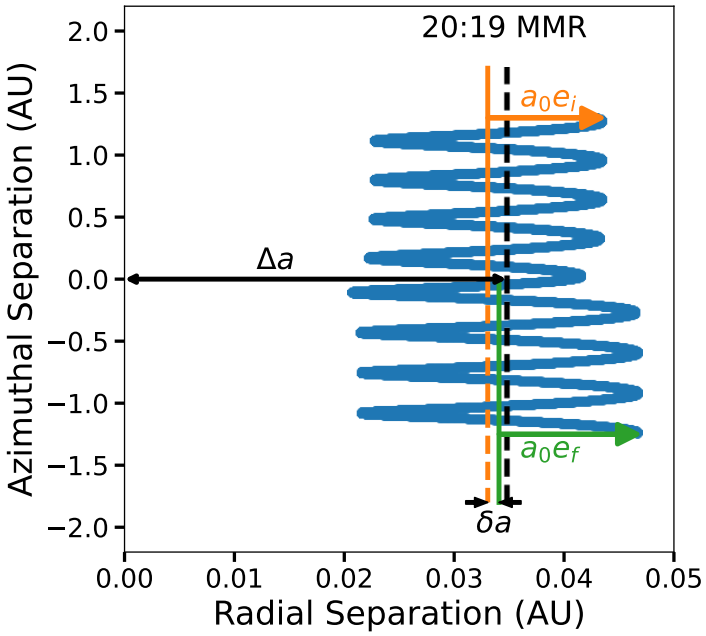

Figure 2.2: Trajectory of a test particle near the 20:19 mean motion resonance (dashed black line) in Hill's coordinates in a frame rotating at the angular rate n_p. In this frame, the inner planet that remains fixed at the origin. In this frame, the test particle's position is described in terms of radial separation $x = a - a_p$ (horizontal axis, AU) and azimuthal separation $y = a_p \theta_{\text{rel}}$ (vertical axis, AU). A test particle on a circular orbit traces a vertical path at constant $x = \Delta a$, drifting downward in y due to its slightly slower mean motion. An eccentric test particle follows the blue epicyclic trajectory, oscillating radially with initial amplitude $a_0 e_i$ while drifting downward in azimuth. Conjunction occurs at $y = 0$, where the gravitational interaction is strongest. After the conjunction, the particle receives a gravitational kick that alters its orbital elements, increasing its semi-major axis and thereby changing its radial oscillation amplitude to $a_0 e_f$. The effective interaction zone is limited to $|y| \lesssim \Delta a$. Reproduced from Tamayo and Hadden (2025) [18]

.

longitudes to change by 2π:

$$t_{\text{conj}} = \frac{2\pi}{\Delta n}, \tag{2.3.4}$$

where $\Delta n = n - n_p$ is the difference in mean motions. Using Kepler's third law to

express $\Delta n/n \approx \frac{3}{2} e_c$ (through Eq. 2.2.5), we can rewrite

$$t_{\text{conj}} = \frac{2}{3}\frac{P}{e_c} \tag{2.3.5}$$

where P is the period of the inner planet. For small e_c corresponding to closely spaced orbits (small Δa), this time between subsequent conjunctions becomes very large.

The second important timescale is the length of the encounter itself. Unlike the time between subsequent conjunctions t_{conj}, this timescale remains short regardless of the period ratio [18].

If the test particle's eccentricity is small ($e \ll e_c$), the planets reach their minimum separation distance at conjunction, where their separation is $x \approx \Delta a$ and the azimuthal displacement is $y = 0$. The gravitational force varies as the inverse square of the separation between the planets. Thus, within an azimuthal range $|y| \lesssim \Delta a$, the force remains approximately constant (within a factor of two), but beyond this range it falls off rapidly [18]. We can therefore use a characteristic interaction timescale Δt_{int}, corresponding to the time during which $|y| \lesssim \Delta a$ and the gravitational interaction remains significant.

The characteristic interaction time Δt_{int} is the time it takes for the angular separation y to change by Δa in the rotating frame, where the outer body moves at a relative velocity $\dot{y} \approx a_p \Delta n$:

$$\Delta t_{\text{int}} \sim \frac{\Delta a}{a_p \Delta n} = \frac{P}{3\pi}. \tag{2.3.6}$$

Notably, Δt_{int} is independent of the orbital separation e_c and is much shorter than t_{conj}.

Because of the strong separation between timescales Δt_{int} and t_{conj}, we can approximate the gravitational interaction as an instantaneous kick at each conjunction, with the bodies following unperturbed Keplerian motion between encounters [3].

2.4 Pendulum Approximation

In addition to the Hill approximation, we also assume the particle's eccentricity remains approximately constant over many conjunctions with typical fractional variations of only a few percent [18]. Under this assumption, called the pendulum approximation, the dynamics reduce to those of a simple pendulum [13].

This assumption simplifies the dynamics considerably, although it breaks down when the eccentricity becomes very small, where even small kicks lead to large fractional changes in mean motion (for a more detailed discussion, see [18]).

Chapter 3

Dynamical Effects of Repeated Conjunctions

Having established the system's geometry in the Hill limit, we now examine how the gravitational kicks at conjunctions affect its dynamics over time. We begin with the non-resonant case, where gravitational kicks occur at varying orbital locations and average out over time. We then turn to mean motion resonances (MMRs), where conjunctions recur at fixed azimuthal angles, allowing the kicks to accumulate coherently and drive long-term dynamical evolution.

3.1 The Typical Case

In the Hill limit, where the planets follow unperturbed Keplerian orbits between conjunctions, the time between successive conjunctions is given by t_{conj} as defined in Sec 2.3.

The angular location of the next conjunction then changes by

$$\Delta\theta = n_1 t_{\text{conj}} = n_2 t_{\text{conj}}. \tag{3.1.1}$$

At each conjunction, the planets exchange energy and their mean motions change, effectively instantaneously. As can be explained from physical grounds (e.g. [15, 18]), for an eccentric test particle orbit, conjunctions happening to the left of the line of apses (left panel of Fig. 3.1) cause the test particle's mean motion to speed up, while those to the right cause it to slow down. For closely separated orbits, Δn is small, and $\Delta\theta$ is therefore big (see Eq. 3.1.1). For most values of $\Delta\theta$ then, subsequent conjunctions occur at arbitrary locations that over time densely fill the 2π radians in azimuth.

This leads to a sequence of positive and negative kicks to the test particle's mean motion that effectively average out over long timescales. In this picture, the gravitational effects due to the planets' orbital motions can be effectively

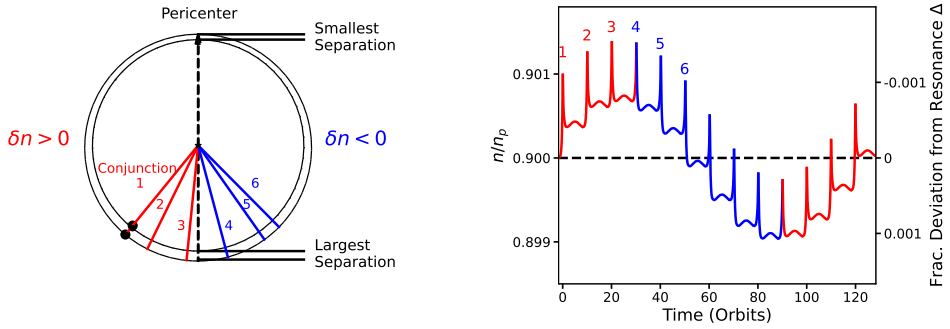

Figure 3.1: Evolution of conjunction geometry and mean motion for a test particle near the 10:9 MMR. The inner planet moves on a fixed circular orbit, while the outer test particle follows an eccentric orbit with a fixed pericenter direction (upward in the left panel). Conjunctions are labeled 1–6, with each line indicating the azimuthal alignment of the two bodies. Conjunctions occurring to the left of the line of apses (vertical dashed line) cause the test particle's mean motion to increase (red), while those to the right cause it to decrease (blue). See the text for a more detailed discussion. The right panel shows the evolution of the mean motion over a full cycle of the system's dynamics. The sequence of gravitational kicks causes the mean motion to oscillate around the resonant value, analogous to the motion of a pendulum. The fractional deviation from exact resonance is indicated on the rightmost side of the plot. Reproduced from Tamayo and Hadden (2025) [18].

ignored, and one can average over the fast orbital motions (smearing out the planets' mass along their respective orbits like a movie played at 100x speed) to analyze slower 'secular' variations in the orbital elements [13].

3.2 Mean Motion Resonances

An important exception occurs when the system lies near a mean motion resonance (MMR), i.e., when the planets' orbital periods form an integer ratio. The strongest MMRs are first-order MMRs of the form p:$p-1$.

Let us take as an example the 10:9 MMR, and as a first pass, begin by ignoring the interactions at conjunction. If the planets begin at conjunction at some azimuthal angle θ, then after 10 orbits of the inner planet, the outer test particle completes exactly 9 orbits, and the two planets have their next conjunction at exactly the same location. Turning on the gravitational interaction between the planets, such a resonance in principle allows the small perturbations at each conjunction to build up coherently, leading to much larger cumulative effects.

The complication is that these interactions slightly change the mean motion

of the test particle, which perturbs the ratio slightly off the resonant value. If the test particle is now moving slightly too fast or slightly too slow (relative to the resonant value), subsequent conjunctions will occur at nearly—but not exactly—the same location. One therefore has to consider the coupled evolution of how the conjunction location and mean motion change with time.

One advantage is that, because the individual kicks are small, the changes to the conjunction location θ are very small from one conjunction to the next. One can therefore approximate this conjunction angle θ as a continuously varying quantity. For a $p:p-q$ MMR, the standard approach is to define the angle

$$\theta \equiv \frac{p\lambda - (p-q)\lambda_p - q\varpi}{q} \overset{\text{at conjunction}}{=} \lambda_{\text{conj}} - \varpi, \tag{3.2.1}$$

where ϖ is the longitude of pericenter of the test particle (e.g. [13]). This makes θ well defined even between conjunctions, but one can see that at conjunction, where by definition $\lambda = \lambda_p = \lambda_{\text{conj}}$, θ corresponds to how far conjunction occurs from the test particle's pericenter (Fig. 3.2).

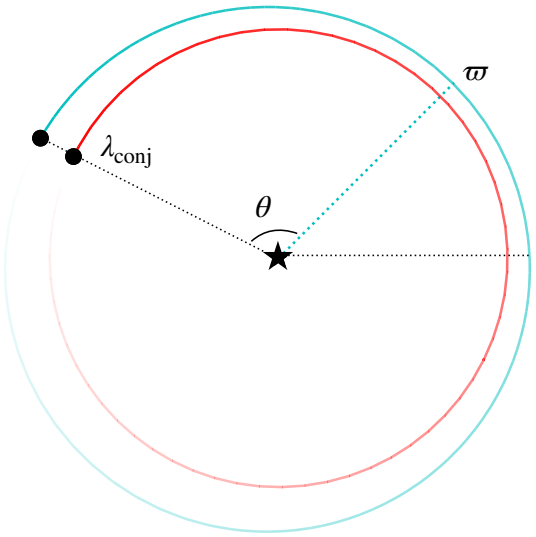

Figure 3.2: Definition of the resonant angle θ at conjunction. The outer test particle (blue orbit) and inner planet (red orbit) are shown at the moment of conjunction, when they share the same mean longitude λ_{conj}. The angle θ is defined as the difference between the conjunction longitude and the longitude of pericenter ϖ of the test particle.

This continuous formulation is useful for analyzing the evolution of the system as it allows us to move beyond a discrete map to a smooth dynamical model.

Taking two time derivatives of θ and replacing p/q in favor of e_c through Eq. 2.2.5 yields

$$\ddot{\theta} = \frac{d^2}{dt^2}\Big(\frac{2}{3e_c}(\lambda - \lambda_p) + \lambda_p - \varpi\Big) = \frac{2}{3}\frac{\dot{n}}{e_c}. \tag{3.2.2}$$

Note that since the outer body is a massless test particle, the planet moves at a constant mean motion $n_p = \dot{\lambda}_p$, so $\dot{n}_p = 0$. Following the argument from [18], we have approximated $\dot{\varpi} = 0$. Given Eq. 3.2.2, we can determine the dynamics of θ provided we find an expression for $\dot{n}$ in terms of θ.

Formally, $\dot{n}$ is infinite under a discrete kick. In order to obtain the differential equation 3.2.2 in an analytically tractable form, we develop a continuous model for $\dot{n}$. We can approximate a continuous function for $\dot{n}$ by imagining we smear the small, discrete kick δn at conjunction over the entire time interval between conjunctions:

$$\dot{n} \approx \frac{\delta n}{t_{conj}} \approx \frac{3}{4\pi} e_c n \delta n. \tag{3.2.3}$$

This approximation is valid under the assumption that the inner planet's mass is sufficiently small and the orbits are sufficiently well separated such that the fractional change in mean motion at each conjunction remains small. As Fig 3.1 illustrates, under these conditions the mean motion exhibits a smooth, sinusoidal variation when averaged over short-timescale fluctuations.

Substituting Eq. 3.2.3 for $\dot{n}$ into to Eq. 3.2.2 , we obtain an expression of $\ddot{\theta}$ in terms of θ:

$$\frac{\ddot{\theta}}{n^2} = \frac{1}{2\pi}\frac{\delta n}{n}\Big(\theta\Big) \tag{3.2.4}$$

This expression fully determines the dynamical evolution of θ provided we determine an equation for $\frac{\delta n}{n}$ as a function of θ.

Chapter 4

Model for a Single Conjunction

To specify the dynamical evolution of the system, we begin by modeling the gravitational kick from a single conjunction, $\frac{\delta n}{n}(\theta)$, as laid out in the previous chapter. This chapter examines how the kick strength varies with the azimuthal angle θ at which conjunction occurs. With this, we study the case of a first-order MMR and lay the groundwork for the analysis of higher-order resonances in the next chapter.

4.1 Fourier Expansion for the Change in Mean Motion at Conjunction

An eccentric test particle orbit introduces an asymmetry by causing the orbital separation to vary with azimuthal angle θ (Fig. 3.2); as a result, we expect the strength of the kick to also depend on the angle at which conjunction occurs. Given that this function must clearly be periodic in θ (the kick is the same at θ and $\theta + 2\pi$), it can be expressed as a Fourier series. The series coefficients were worked out explicitly by Namouni et al (1996), but we differ from their approach by defining θ to be measured from the location where the orbits are closest[1] [14]. For eccentricities not too close to zero[2], this yields

[1] This causes all the Fourier amplitudes to be positive, instead of alternating between even and odd terms [18].

[2] The leading order perturbation calculation proceeds by calculating the changes to the orbital elements along unperturbed Keplerian orbits. In the case of circular orbits, the symmetry before and after encounter predicts no net exchange of energy, and thus no change to the mean motion. This therefore requires doing perturbation theory to second order in the masses to capture the small change from a circular orbit during a single conjunction, which yields $\delta n/n \approx -\frac{\pi^2 A_1^4 \mu^2}{e_c^5}$. At all but the smallest eccentricities, this term is negligible due to the extra factor of μ—see [18] for a discussion of the value of the eccentricity at which this happens.

MMR Order	A_q
1	0.845
2	0.754
3	0.748
4	0.778
5	0.832
6	0.904
7	0.995
8	1.104
9	1.235
10	1.388

Table 4.1: Numerical prefactors A_q for MMRs of order q. They arise from the leading-order term in a Taylor expansion of MMR strengths in powers of the normalized eccentricity $\tilde{e}$ [6]. Table reproduced from Tamayo and Hadden (2025) [18].

$$\frac{\delta n}{n} = 2\pi \frac{\mu}{e_c^2} \sum_{m=1}^{\infty} \sum_{k=1}^{\infty} D_k(m) \sin(m\theta). \tag{4.1.1}$$

We show in Appendix B that for small eccentricities ($e_c \lesssim 0.4$) infinite series in k can be approximated by its first term $D_1 = mA_m^2 \tilde{e}^m$, where we express the Fourier amplitudes in terms of numerical coefficients A_m^2 (see Table 4.1). These terms differ by a numerical factor from those used by Namouni et al. but later lead to simpler expressions for the resonance widths and libration frequencies [18]. This simplification yields

$$\frac{\delta n}{n} \approx 2\pi \frac{\mu}{e_c^2} \sum_{m=1}^{\infty} mA_m^2 \tilde{e}^m \sin(m\theta). \tag{4.1.2}$$

The fractional change to the test particle's mean motion at conjunction depends on the perturbing planet's mass (relative to the dominant central mass) $\mu \equiv M_p/M_\star$, as well as the orbital separation. We quantify the latter through the value of the eccentricity at which the orbits start to cross e_c (as defined using Eq. 2.2.2 and 2.2.5). We see that the Fourier amplitudes $mA_m^2 \tilde{e}^m \sin(m\theta)$ scale as powers of the normalized eccentricity. Thus, for low eccentricities $\tilde{e} << 1$, only the first few terms of the Fourier series are significant and higher orders can be safely neglected.

A key point is that the size of these kicks is independent of which MMR the planets are in, or whether they are in any MMR at all. Instead, we will show that this Fourier expansion can explain the various well-known scalings of MMRs of different orders.

As a numerical check in Fig. 4.1, we initialize a suite of numerical integrations in REBOUND with an eccentric test particle perturbed by a massive ($\mu = 3.75\times10^{-10}$) planet on an interior, circular orbit. The initial period is always chosen as $P_2/P_1 = 1.015$, which positions the bodies well within the closely spaced Hill limit, but outside any strong (low-order) MMRs. Each integration is set up so that a single conjunction happens at a different θ, and we numerically evaluate the resulting fractional change to the test particle's mean motion $\delta n/n$ due to the single gravitational encounter (blue solid line). The top panel uses a test particle eccentricity $\tilde{e} = 0.1$, while the bottom panel uses a higher eccentricity $\tilde{e} = 0.4$. In the top panel, we see that the numerical results (solid blue line) closely match the sine curve shape of the first term in the Fourier series (orange dotted line), while the sum of the first four terms (dashed purple line) is visually indistinguishable from the integration. The key physical insight is then that, for low eccentricities, the fractional change to the mean motion imparted by a single conjunction always scales approximately linearly in the eccentricity.

As orbital eccentricity increases, the contribution of higher order terms becomes larger and the first-order approximation $\frac{\delta n}{n} \approx 2\pi \frac{\mu}{e_c^2} A_1^2 \tilde{e} \sin(\theta)$ is no longer valid as more terms in the Fourier series are needed to match the results of the simulation. As the bottom panel illustrates, when $\tilde{e} = 0.4$ the first four terms in the series are roughly of the same order so the first order sine curve is no longer a good approximation.

4.2 First Order MMRs

If we substitute the leading order term of the kick to the mean motion (Eq. 4.1.2) into our differential equation for θ (Eq. 3.2.4), we obtain an expression of the form

$$\ddot{\theta} = -C\sin\theta, \tag{4.2.1}$$

which is the differential equation of a pendulum with Hamiltonian

$$H = \frac{\dot{\theta}^2}{2} + C\cos\theta. \tag{4.2.2}$$

The "strength" coefficient C for this $\cos\theta$ potential is given by

$$C = A_1^2 \frac{\mu m^2}{e_c^2}\tilde{e}, \tag{4.2.3}$$

where the numerical coefficient A_1 is given in Table 4.1.

We see that this strength of the resonance potential, which would traditionally come from identifying the appropriate term in the disturbing function expansion of the gravitational potential between the two planets, scales linearly with the eccentricity as expected for a first-order MMR [13].

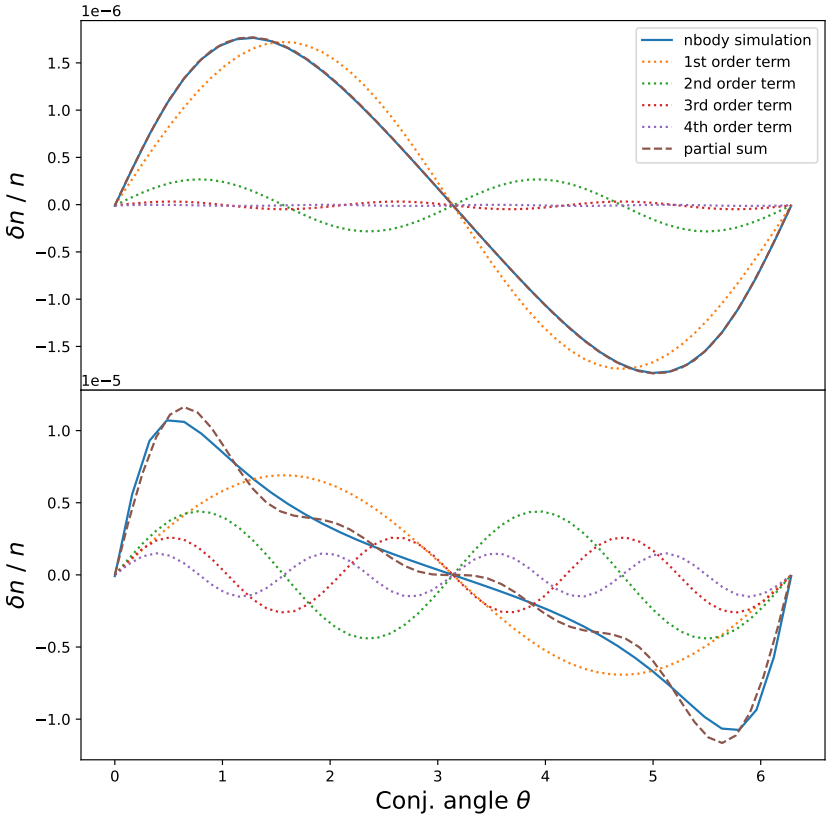

Figure 4.1: Fourier decomposition of the fractional change in mean motion $\delta n/n$ as a function of conjunction angle θ, compared to results from direct N-body simulations in REBOUND. The blue solid line shows the numerical result from a single conjunction, where a test particle is perturbed by a massive planet on a circular orbit with $\mu = 3.75 \times 10^{-10}$ and orbital period ratio $P_2/P_1 = 1.015$. The first four individual Fourier terms are plotted as dotted lines in orange, green, red, and purple, respectively; the dashed brown line shows their sum. **Top panel:** For small eccentricity ($\tilde{e} = 0.1$), the first-order term (orange) closely matches the numerical result. **Bottom panel:** At higher eccentricity ($\tilde{e} = 0.4$), higher-order terms contribute significantly, and multiple terms are required to reproduce the simulation.

However, while in the traditional approach there is a different numerical coefficient for each p:$p-1$ MMR (see Appendix of [13]), we see that in the compact

limit, these differences can be expressed in terms of the fractional separation between the orbits e_c and an order-unity coefficient A_1 that is common to all first-order MMRs [6, 18].

This result is also physically plausible. It seems intuitive that an effect caused by the asymmetry introduced by an eccentric orbit would, for small eccentricities, scale linearly in the eccentricity. But if all conjunctions lead to changes in the mean motion that scale linearly in the eccentricity, why wouldn't MMRs of all orders have strengths of $\mathcal{O}(\tilde{e})$?

Chapter 5

Higher Order MMRs

While first-order MMRs involve a single conjunction per resonant cycle, higher-order resonances feature multiple encounters, whose combined effects determine their overall strength. In this chapter, we extend our analysis to higher order MMRs and show how the geometry of these multiple kicks leads naturally to the well-known e^q scaling of resonance strength. This approach provides a simple and intuitive geometric explanation for this central result in celestial mechanics.

5.1 Pendulum Dynamics for Higher Order MMRs

We now wish to consider a qth order p:$p-q$ MMR. In the time the inner planet completes p orbits, the outer planet completes p–q orbits. After one such interval–one cycle– the planets return to conjunction at the same azimuthal angle θ, since both have completed an integer number of orbits.

Within each cycle, however, additional conjunctions now occur. Because the inner planet completes q more orbits than the outer planet during a cycle, it must overtake the outer planet q times. In other words, there are q total conjunctions per cycle.

While the final conjunction in the cycle always occurs at the original location θ after an integer number of orbits, the other $q-1$ conjunctions will in general occur after only a fractional number of orbits at intermediate longitudes spaced around the orbit. We investigate the specific locations of these conjunctions in Sec. 5.2.

In the regime where perturbation theory is useful, the dynamical evolution builds up over many p:$p-q$ cycles. To make analytical progress, we therefore assume that the mean longitudes advance at their unperturbed rates, and that the other orbital elements remain fixed over a p:$p-q$ cycle in order to calculate the *net* change to the test particle's mean motion $\left(\frac{\delta n}{n}\right)_{\text{cycle}}$ from the q conjunctions.

In essence, we move to considering a discrete mapping from one p:$p-q$ cycle to the next, rather than from each individual conjunction to the next as we did in Sec 3.2.

Our goal is then to use the fact that we assume the changes are small from one mapping step to the next to again obtain a smoothed model with a differential equation we can solve, analogous to Sec. 3.2. Following the logic in that section, we obtain a similar differential equation to Eq. 3.2.2,

$$\frac{\ddot{\theta}}{n^2} = \frac{1}{2\pi q}\left(\frac{\delta n}{n}\right)_{\text{cycle}} \tag{5.1.1}$$

where now $\left(\frac{\delta n}{n}\right)_{\text{cycle}}$ is the net change in mean motion due to all q kicks in a single cycle,

$$\left(\frac{\delta n}{n}\right)_{\text{cycle}} = \sum_{k=1}^{q} \frac{\delta n}{n}\left(\theta_k\right). \tag{5.1.2}$$

where θ_k is the angle at which the kth conjunction occurs. The additional factor of $\frac{1}{q}$ included in Eq. 5.1.1 accounts for the fact that the sum represents the total cycle kick, so we divide by q to obtain the average contribution per conjunction.

Substituting in the expression for a single kick from Eq. 4.1.2 yields

$$\left(\frac{\delta n}{n}\right)_{\text{cycle}} = \sum_{k=0}^{q-1}\sum_{m=1}^{\infty} B_m \sin\left[m\theta_k\right] \tag{5.1.3}$$

where

$$B_m = 2\pi \frac{\mu}{e_c^2} m A_m^2 \tilde{e}^m. \tag{5.1.4}$$

We thus obtain a sum over q conjunctions, each of which is an infinite sum over Fourier modes. Given that we assume $\tilde{e}$ is small, the B_m shrink rapidly with increasing m. This hierarchy makes it valuable to interchange the order of summation and exploit the fact that we are approximating the B_m as equal for each conjunction within the cycle,

$$\left(\frac{\delta n}{n}\right)_{\text{cycle}} = \sum_{m=1}^{\infty} B_m \left(\sum_{k=0}^{q-1} \sin\left[m\theta_k\right]\right). \tag{5.1.5}$$

This reorganizes the outer sum in terms of $B_m \propto \tilde{e}^m$ so that we can easily identify the leading order terms in the series, and highlights that the inner sum is reduced to a geometric factor that only depends on the q locations of conjunction θ_k within a cycle.

5.2 Conjunction Locations within a Cycle

To evaluate Eq. 5.3.2 and determine the net effect of the q kicks occurring during a cycle, we must identify the azimuthal locations θ_k of each conjunction along with their integer multiples $m\theta_k$. In this section, we use examples to deduce the general result, but a complete derivation of the general result is provided in Appendix A.

Throughout this analysis we assume the inner planet's mass is small and the orbits are sufficiently widely spaced such that variations in the test particle's mean motion n are small. That is, the amplitude of the smooth oscillations in n (i.e. the sine curve shape in Fig 3.1) remains small over the course of many cycles. Under this approximation, we set the test particle's mean motion to its exact resonant value, $n = n_{res}$. With both planets traveling at constant angular speed, the conjunctions occur at equally spaced intervals in time (where t_{conj} is defined in Eq. 2.3.4, but now $\Delta n = n_{res} - n_p$ = constant).

Recall from Sec. 5.1 that a cycle corresponds to the interval in which the inner planet completes p full orbits. Thus, over the course of one cycle, the inner planet travels a total angular distance of $2\pi p$. Since there are q conjunctions per cycle and these conjunctions are equally spaced in time, the angular separation between successive conjunctions is

$$\Delta\theta = \frac{2\pi p}{q}. \tag{5.2.1}$$

It follows that the kth conjunction (starting from the reference angle θ) occurs at

$$\theta_k = \theta + k\Delta\theta \tag{5.2.2}$$

where k ranges from 1 to q.

In general, the offset $k\Delta\theta$ is not an integer multiple of 2π, so these conjunctions occur at various longitudes around the orbit. Only when $k = q$ (corresponding to the final conjunction in the cycle) does the angular displacement become $2\pi p$, returning the system to its original configuration and completing the cycle.

Locations of θ_k

Because the ratio $p/q > 1$, the angular separation between conjunctions $\Delta\theta$ is always greater than 2π. The inner planet completes more than one full orbit before overtaking the outer planet again. As a result, it is not immediately obvious where the next conjunction occurs in relation to the original angle θ.

As a concrete example, consider a $7:2$ MMR, where there are $7-2=5$ conjunctions per cycle. From Eq. 3.1.1, the angular displacement between succes-

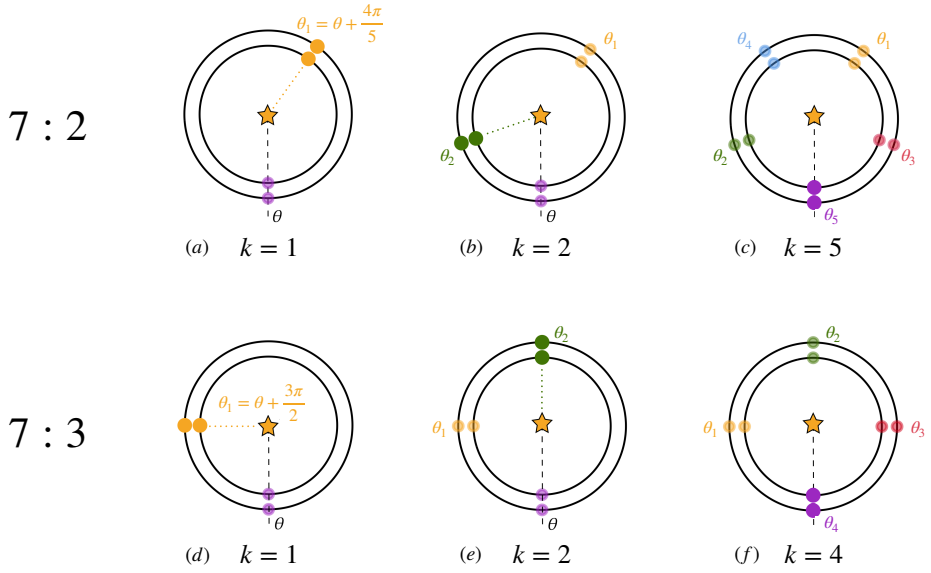

Figure 5.1: Azimuthal locations θ_k of successive conjunctions within a cycle, shown for the 7:2 (top row) and 7:3 (bottom row) MMRs. In each case, the planets orbit counterclockwise. Conjunctions are marked by colored dots (orange for $k = 1$, green for $k = 2$, red for $k = 3$, blue for $k = 4$, and purple for $k = 5$), with k indicating the conjunction number within the cycle. **Top row (7:2 MMR):** Five conjunctions occur per cycle, with angular separation $\Delta\theta = 14\pi/5$. Panels (a) and (b) show the first two locations, respectively, and panel (c) shows all five, spaced evenly by $2\pi/5$ rad. **Bottom row (7:3 MMR):** Four conjunctions occur per cycle with step size $\Delta\theta = 7\pi/2$, producing evenly spaced points at $2\pi/4$ rad intervals, as shown in panel (f). In both cases, the q conjunctions occur at azimuthal angles evenly spaced by $2\pi/q$, a general result for any p:$p-q$ MMR (see Appendix A).

sive conjunctions is

$$\Delta\theta_{7:2} = \frac{14\pi}{5}. \tag{5.2.3}$$

We compute the first conjunction as $\theta_1 = \theta + \Delta\theta$. On a polar plot, this angle wraps around the circle more than once: the planet completes two full revolutions and proceeds an additional $4\pi/5$ rad beyond θ (panel (a) in Fig 5.1). The second conjunction occurs another $14\pi/5$ rad beyond that, again wrapping around and landing $4\pi/5$ rad from θ_1 (panel b). Continuing this process for all five conjunctions within the cycle (panel c), the points $\theta_1, \ldots \theta_5$ are found to be evenly spaced around the circle, each separated by $2\pi/5 = 2\pi/q$ rad.

A similar pattern arises in the 7 : 3 MMR, where there are $7-3=4$ conjunctions per cycle. In this case, the angular distance between conjunctions is

$$\Delta\theta_{7:3} = \frac{7\pi}{2} \tag{5.2.4}$$

corresponding to one full revolution plus an additional $3/2\pi$ rad. The first conjunction therefore occurs $3\pi/2$ rad counterclockwise from θ (panel (d) in Fig. 5.1), and each subsequent conjunction advances by the same angular amount (panel e). After plotting all four conjunctions in the cycle (panel f), we again find them evenly spaced by $2\pi/4 = 2\pi/q$ rad.

In both examples, despite this large step size $\Delta\theta$, the spatial separation between successive conjunctions is always $2\pi/q$. As demonstrated in Appendix A, this result holds generally for any $p : p-q$ MMR.

This result illustrates that the gravitational kicks during a cycle occur at evenly spaced locations around the orbital path. Qualitatively from Fig 4.1, we can see that conjunction angles on opposite sides of the orbit result in kicks of opposite signs, so that they partially cancel each other. This symmetry leads to cancellation among the first few terms in the resulting Fourier series. In the Section 5.3 we show that the net effect of these q kicks vanishes up to order e^{q-1}, with the first nonzero contribution appearing at order e^q.

Locations of $m\theta_k$ for Higher Fourier Modes ($m > 1$)

Recall that our goal is to evaluate Eq. 5.3.2, which computes the total kick to the mean motion over a cycle for a given Fourier mode m. This expression involves the angles $m\theta_k$ which are integer multiples of θ_k.

To determine the spatial distribution of the angles $m\theta_k$ within a cycle, we again begin with the 7:2 MMR. For $m = 1$, we have already seen that the conjunction angles θ_k are evenly spaced by $2\pi/5$ rad (panel (a) of Fig 5.2).

Now consider $m = 2$. The angular distance between successive $m\theta_k$ becomes $2\Delta\theta_{7:2} = 2\cdot\frac{14\pi}{5} = \frac{28\pi}{5}$. That is, the planet wraps around the circle four times and proceeds an additional $8\pi/5$ rad beyond θ. Each subsequent $m\theta_k$ angle advances by the same amount. The resulting set of angles $m\theta_k$ again forms five evenly spaced points around the circle, as shown in panel (b) of Fig 5.2. These angles exactly match the conjunction locations θ_k; the only difference is the order in which they occur within the cycle, indicated in the figure by the labeled indices 1-5.

We repeat this analysis for $m = 3$ and $m = 4$ (panels c and d), and again find that the set of angular locations remains the same. Only the ordering of the angles is affected.

A qualitatively different result arises when $m = q = 5$. In this case, the angular distance between conjunctions becomes $5\Delta\theta_{7:2} = 5\cdot\frac{14\pi}{5} = 14\pi$, which is an exact

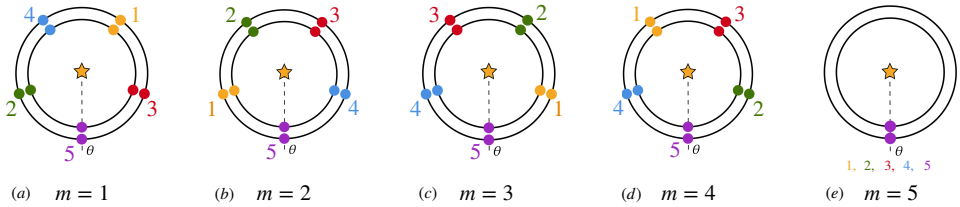

(a) $m = 1$ (b) $m = 2$ (c) $m = 3$ (d) $m = 4$ (e) $m = 5$

Figure 5.2: Angular locations of the conjunction angles multiplied by Fourier mode number m, shown for the 7:2 mean motion resonance. In all panels, the five original conjunction angles θ_k (for $k = 1$ to 5) are plotted around the orbit, with the ordering of each $m\theta_k$ indicated by color and label. **Panel (a):** For $m = 1$, the configuration matches that of Fig. 5.1. **Panels (b–d):** For $m = 2, 3, 4$, the angular locations $m\theta_k$ remain evenly spaced around the orbit, but their order is permuted within the cycle, as shown by the changing sequence of colors. **Panel (e):** For $m = q = 5$, all $m\theta_k$ coincide at the angle θ.

multiple of 2π. Consequently, all values $m\theta_k$ coincide at the original angle θ, as illustrated in panel (e).

In Appendix A, we generalize these results to arbitrary $p : p-q$ MMRs. Specifically:

- When $m < q$, the angles $m\theta_k$ are spaced uniformly around the unit circle by $2\pi/q$.
- When $m = q$, all $m\theta_k$ coincide at θ.

These results extend to $m > q$ as well (see Appendix A). In general:

- **Case 1:** When m is not an integer multiple of q: the angles $m\theta_k$ are spaced uniformly around the unit circle by $2\pi/q$.
- **Case 2:** When m is an integer multiple of q, all $m\theta_k$ coincide at θ.

In both cases, the value of m affects only the ordering that the angles appear within the cycle, not the angles themselves. This does not affect the result of Eq. 5.3.2, as it merely corresponds to permuting the order of terms in the sum.

5.3 Summing Kicks within a Cycle

We are now in a position to compute Eq. 5.1.5, the total change in mean motion over one cycle.

First, it is helpful to isolate the contribution of a single mode m to this total cycle kick:

$$\left(\frac{\delta n}{n}\right)_{\text{cycle},m} = B_m \sum_{k=0}^{q-1} \sin(m\theta_k) = B_m \sum_{k=0}^{q-1} \text{Im}\left[\exp\{(im\theta_k)\}\right] \tag{5.3.1}$$

where we have expressed $\sin(m\theta_k) = \text{Im}\left[\exp\{(im\theta_k)\}\right]$ in the second step.

This formulation reveals a useful geometric interpretation: each term in the sum is the imaginary part of a complex vector of magnitude B_m, oriented at angle $m\theta_k$ on the unit circle. Each vector corresponds to the mth Fourier-mode contribution from one of the q conjunctions. The total contribution from mode m can then be computed geometrically by adding the imaginary (vertical) components of these vectors.

Depending on whether m is evenly divisible by q, these vectors adopt one of two distinct spatial configurations described in Sec 5.2. We analyze each case separately below.

Case 1: Fourier mode m is not an integer multiple of q

If m is not divisible by q, the angles $m\theta_k$ are spaced uniformly around the unit circle by $2\pi/q$ (see Sec. 5.2). This configuration is illustrated for the 7:2 MMR example in panel (a) of Fig 5.3. The sum of the imaginary (vertical) components of the corresponding vectors can be inferred from the symmetry. Since the vectors are evenly spaced about the circle, their center of mass lies at the origin and their sum vanishes. Equivalently, adding the vectors head-to-tail yields a closed regular polygon[1] which sums to zero (panel (b) of Fig. 5.3).

Formally, using $\theta_k = \theta + 2\pi k/q$, we write Eq. 5.3.2 as

$$\left(\frac{\delta n}{n}\right)_{\text{cycle},m} = B \cdot \text{Im}\left[\exp\{(im\theta)\} \sum_{k=0}^{q-1} \exp\left\{(i\frac{2\pi mk}{q})\right\}\right]. \tag{5.3.2}$$

The term $\sum_{k=0}^{q-1} \exp\left\{(i\frac{2\pi mk}{q})\right\}$ is a sum over the qth roots of unity, which evaluates to zero whenever m is not divisible by q. This is a standard result in complex analysis and number theory [20].

We therefore conclude:

$$\left(\frac{\delta n}{n}\right)_{\text{cycle, } m \text{ is not multiple of } q} = 0 \tag{5.3.3}$$

so Fourier modes m not divisible by q cancel over the cycle and have no contribution to the mean motion kick.

[1] Though different values of m permute the sequence of angles θ_k, the order in which the vectors are added does not matter. Changing the order in which the vectors are added produces distinct regular star polygons, all of which are closed and sum to zero. A more detailed discussion of these configurations is provided in Appendix A.1.

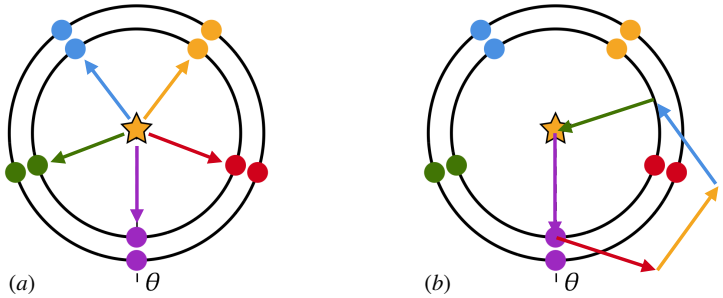

Figure 5.3: Geometric interpretation of the Fourier sum over kicks in a mean motion resonance cycle, shown for the case where the Fourier mode number m is not divisible by q (specifically, the 7:2 MMR with $q = 5$). **Panel (a):** Each arrow represents a complex vector with angle $m\theta_k$, corresponding to one term in the sum of Eq. 5.3.2. The five vectors are spaced uniformly around the unit circle by $2\pi/q$ and point in directions determined by the angles $m\theta_k$. **Panel (b):** Adding the vectors head-to-tail yields a closed regular polygon. As a result, their vertical components cancel exactly and the total contribution to the mean motion kick from this mode vanishes. This configuration corresponds to a sum over the qth roots of unity, which always vanishes when m is not a multiple of q [20].

Case 2: Fourier mode m is an integer multiple of q

If m is an integer multiple of q, then all angles $m\theta_k$ coincide at θ. In this case, the complex vectors corresponding to Eq. 5.3.2 all point in the same direction and add constructively.

The imaginary component of each vector contributes $B_m \sin\theta$ to the sum, so the total contribution from mode m is

$$\left(\frac{\delta n}{n}\right)_{\text{cycle, } m \text{ is multiple of } q} = qB\sin\theta \tag{5.3.4}$$

$$= 2\pi\frac{\mu}{e_c^2} m q^2 A_m^2 \tilde{e}^m \sin\theta. \tag{5.3.5}$$

This geometric reasoning shows that only specific Fourier modes contribute to the cumulative effect of multiple conjunctions in a cycle: all modes not divisible by q cancel out due to symmetry, while those that are align constructively. We can now combine these results to derive a general expression for the net kick per cycle and recover the familiar eccentricity scaling of MMRs.

5.4 Recovering the e^q Scaling of MMR Strength

From the analysis in the previous section, we conclude that only Fourier modes for which m is an integer multiple of q contribute to the net kick to mean motion over a cycle (Eq. 5.3.2). Substituting these nonzero terms into the full Fourier expansion Eq. 5.1.5, the total fractional change in mean motion over a cycle becomes

$$\frac{\delta n}{n}\Big(\theta\Big)_{\text{cycle}} = 2\pi\frac{\mu}{e_c^2}\sum_{n=1}^{\infty}(nq)A_{nq}^2\tilde{e}^{nq}\cdot\sin(nq\theta) \tag{5.4.1}$$

For small eccentricities, terms with $n > 1$ decay rapidly due to the steep falloff of $\tilde{e}^{nq}$, especially for high order resonances with large q. Therefore, the series is strongly dominated by the $n = 1$ term.

To leading order in eccentricity, we thus obtain

$$\frac{\delta n}{n}\Big(\theta\Big)_{\text{cycle}} \approx 2\pi\frac{\mu}{e_c^2}qA_q^2\tilde{e}^q\sin(q\theta) \tag{5.4.2}$$

showing explicitly that the amplitude of the total cycle kick scales as e^q (recall that $\tilde{e}\propto e$ from Eq. 2.2.1).

From Eq. 4.2.1, the strength C of the MMR in the pendulum approximation is defined by the equation of motion $\ddot{\phi} = -C\sin\phi$ where $\ddot{\theta} = \ddot{\phi}/q$ is related to $\left(\frac{\delta n}{n}\right)_{\text{cycle}}$ in Eq. 5.1.1. We perform the change of variables

$$\frac{\ddot{\phi}}{n^2} = q\frac{\ddot{\theta}}{n^2} \tag{5.4.3}$$

to obtain the pendulum form for the equation of motion. Substituting the leading-order kick into this expression yields

$$C = \mu\Big(\frac{nqA_q}{e_c}\Big)^2\tilde{e}^q. \tag{5.4.4}$$

This recovers the well-known result that, to leading order in eccentricity, the strength of a $p:p-q$ MMR scales as e^q.

Furthermore, the only higher harmonics that contribute to the total cycle kick are those with amplitudes scaling with e^{aq} where a is an integer. This result explains why, particularly for high-order resonances, the leading-order term in the strength series provides an excellent approximation to the resonance dynamics.

Chapter 6

Conclusion

In this thesis, we have demonstrated that higher order MMRs are weak because the gravitational kicks from multiple conjunctions within each resonance cycle cancel each other out. This physical and geometric argument provides an intuitive framework for understanding resonance strength, one that complements and simplifies the traditional computationally-intensive perturbation theory approach.

Our analysis operates in the Hill limit, where gravitational interactions between planets can be approximated as discrete kicks applied at conjunctions. We show that for a $p : p - q$ MMR, the net kick to mean motion over the course of a cycle is linearly proportional to the strength of the resonance. This kick can be expressed as a sum of q infinite Fourier series in powers of scaled eccentricity $\tilde{e}$. We showed that the first $q - 1$ terms in each series cancel due to the symmetric geometry of the conjunction locations, leaving the leading order term that scales as $\tilde{e}^q$. This cancellation provides a natural geometric explanation for the observed resonance strength scaling result.

Beyond offering an intuitive interpretation for this scaling, the discrete kick framework offers a simple path toward understanding more subtle resonant effects that have recently been found to be important. In particular, MMRs introduce new frequencies into the problem (corresponding to the slow pendulum oscillations), so that the frequencies of any pair of MMRs generically result in additional “secondary" resonances between those new frequencies. This gives rise to a second hierarchy of resonances, independent of the hierarchy in powers of the eccentricity discussed in this paper, now between “primary" resonances (the ones discussed in this thesis), secondary resonances arising from interactions between primary resonances, tertiary resonances from interactions between secondary resonances, etc. While this sequence quickly becomes so weak as to be negligible, secondary resonances have been found to play a key role in driving instabilities in nearly circular orbital configurations [17].

The traditional perturbation theory approach becomes extremely cumber-

some for such secondary resonances. For example, the algebraic expression for the strength of a single such resonance spans four appendices and several pages in [16]. By contrast, the simple model in this thesis of discrete kicks in the Hill limit provides a much simpler physical picture for combining the effects of conjunctions from two separate MMR cycles, and a clear path toward simple expressions for their strengths. Other members in my research group are currently pursuing this direction. So to conclude, this thesis formulates a new intuitive approach to investigating the effects of MMRs that is not only powerful in its own right, but also opens up new avenues for research.

Appendix A

Conjunction Locations θ_k within a Cycle for a General $p:p-q$ MMR

As demonstrated in Sec 5.2, the 5 conjunctions that occur within one cycle of a 7:2 MMR are equally spaced around the orbit by the angle $2\pi/5$. Here, we derive this result for a general $p:p-q$ MMR.

To determine where in space each of the q conjunctions occurs, we consider the angle swept out by the inner planet at each successive conjunction. The total angular distance traveled by the planet grows linearly with each conjunction, but since the planet moves around a circle, we're only interested in its position *around* the orbit — that is, where it is located on the circle, not how far it has traveled in total. We call this circular location the spatial angle θ_k, and it repeats every 2π.

The spatial location of the k^{th} conjunction is found by taking the total angular distance traveled modulo 2π:

$$\theta_k = \left(\frac{2\pi pk}{q}\right) \bmod 2\pi = 2\pi \frac{(pk) \bmod q}{q} \tag{A.0.1}$$

where $k = 1, 2, \ldots, q$ labels successive conjunctions within one cycle.

As an example, consider again the $7:2$ MMR, where there are $7-2=5$ conjunctions per cycle. The spatial angle between subsequent conjunctions (ie taking $k=1$) is

$$\theta_1 = \left(2\pi\frac{7}{5}\right) \bmod 2\pi = \frac{2}{5}(2\pi). \tag{A.0.2}$$

This means that if the first conjunction occurs at θ, the next occurs $2/5$ of the way around the circle from it (see panels (a) and (b) in Fig. 5.1). Continuing through

the full set of 5 conjunctions, we find they are evenly spaced around the orbit, as shown in panel (c).

We now demonstrate that, for a general p:$p-q$ MMR, the set of spatial conjunction angles θ_k in a cycle consists of q equally spaced points on the unit circle.

First, consider the case where p and q are relatively prime (note that at a given period ratio, the lowest order MMR always has relatively prime p and q). When p and q share no common divisors, the sequence $(pk \bmod q)$ for $k = 1, 2 \ldots q$ cycles through each of the q possible remainders exactly once. To see this, suppose that two values $k_1 \neq k_2$ gave the same remainder. If these two values were to give the same remainder, then $p(k_1 - k_2)$ would have to be divisible by q. But since p and q have no common factors, this implies q divides $(k_1 - k_2)$, which is impossible if both k_1 and k_2 lie between 1 and q. Thus, each value of k corresponds to a distinct remainder.

Substituting into Eq. A.0.2 , we see that the spatial conjunction angles θ_k take the values

$$\left\{ \frac{2\pi \cdot 0}{q}, \frac{2\pi \cdot 1}{q}, \ldots, \frac{2\pi \cdot (q-1)}{q} \right\} \tag{A.0.3}$$

in some order. This corresponds to q points uniformly spaced around the orbit, separated by $2\pi/q$ (though not necessarily appearing in increasing angular order, as we saw for the 7:2 MMR example in Fig. 5.1).

Now consider the case were p and q are not relatively prime and share greatest common denominator d. Write $p = d\tilde{p}$ and $q = d\tilde{q}$, so that $\tilde{p}$ and $\tilde{q}$ are coprime. The sequence $(\tilde{p}k \bmod \tilde{q})$ for $k = 1, 2, \ldots, \tilde{q}$ again cycles through all $\tilde{q} = q/d$ distinct remainders.

The corresponding set of spatial angles is then:

$$\left\{ \frac{2\pi d \cdot 0}{q}, \frac{2\pi d \cdot 1}{q}, \ldots, \frac{2\pi d \cdot (q-1)}{q} \right\} \tag{A.0.4}$$

which are q/d distinct points evenly spaced by $2\pi d/q$. These angles repeat d times over the course of the q conjunctions, forming a periodic pattern with d identical segments within a cycle. In this case, the conjunction locations remain uniformly spaced, but with fewer distinct angles and multiple repetitions per cycle.

A.1 Star Polygon Formulation

As shown in the previous section, while the q conjunction angles in a cycle are evenly spaced around the unit circle, they do not necessarily occur in increasing angular order. For instance, for the $7:2$ MMR example from Fig 5.1, if one draws a line sequentially connecting the locations of conjunctions around the circle as they occur in time, the resulting figure is a five-pointed star.

For higher order MMRs with a large number of conjunctions per cycle, there are even more possible permutations of conjunction orderings, and correspondingly a greater variety of "star" shapes that can emerge from this construction. In general, the sequence of conjunction locations within a $p : p - q$ MMR traces out a shape known as a regular star polygon.

A regular star polygon is conventionally denoted by a Schläfli symbol $\{a/b\}$, where a is the number of vertices and b is the so-called density of the polygon [21]. The density of the polygon is the sum of the internal angles at all the vertices divided by 360^o.

For example, 5/1 corresponds to a regular pentagon, while 5/2 is the familiar five-pointed star. The parameters a and b must be relatively prime for the figure to form a single connected shape. When a and b are not coprime, the resulting figure consists of multiple disconnected components, and the symbol reduces to an equivalent coprime form.

As these examples illustrate, the quantity $b-1$ determines how many vertices are skipped when drawing lines between successive points. Therefore, an {a/b} star polygon can be constructed by placing a evenly spaced points on a circle and connecting each point to the point b steps ahead, wrapping around modulo a.

Mapping this concept to a p:$p-q$ MMR, we identify:

- $a = q$, the number of conjunctions in a resonance cycle, and
- $b = p - q$, the number of angular steps between conjunctions

Thus, each p:$p-q$ MMR corresponds to a star polygon {q/(p - q)} that captures the spatial arrangement and temporal ordering of conjunctions within the cycle. Fig. A.1 illustrates several such configurations, labeled with the MMR period ratio as well as the corresponding Schläfli symbol.

An important feature of the results developed in this thesis is that all MMRs of a given order q share the same functional form for the gravitational kick at conjunction, $\frac{\delta n}{n}$. This allows our analysis to depend only on the resonance order q, regardless of the specific period ratio $p/(p-q)$. For example, a 10:7 and 8:5 MMRs are both third-order ($q = 3$) and are treated identically in the dynamical framework we develop.

Here, we see where MMRs of the same order are not entirely identical: the specific values of p and q still influence the ordering of conjunctions within a cycle. In particular, the period ratio determines the polygon density $d = p - q$. This distinction is illustrated in Fig. A.2, which compares the star diagrams of three different 7th order MMRs.

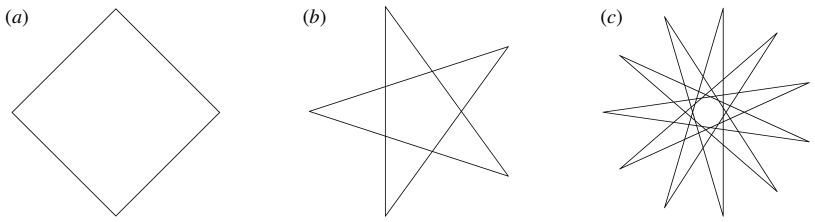

MMR :	5 : 1	7 : 2	13 : 5
Polygon :	{4/1}	{5/2}	{11/5}

Figure A.1: Star polygons corresponding to the sequence of conjunction locations within a resonance cycle for different MMRs. Each diagram connects the conjunction angles in the order they occur during a single p:$p-q$ cycle, forming a regular star polygon {q/d}, where q is the number of conjunctions per cycle and $d = p - q$ is the angular step between them. **(a)** 5:1 MMR $\rightarrow$ {4/1} polygon, a square. **(b)** 7:2 MMR $\rightarrow$ {5/2} polygon, a five-pointed star. **(c)** 13:5 MMR $\rightarrow$ {11/5} polygon, a denser star shape. The shape depends only on the resonance order q and step size d, and illustrates how the temporal ordering of conjunctions results in a geometric structure within the cycle.

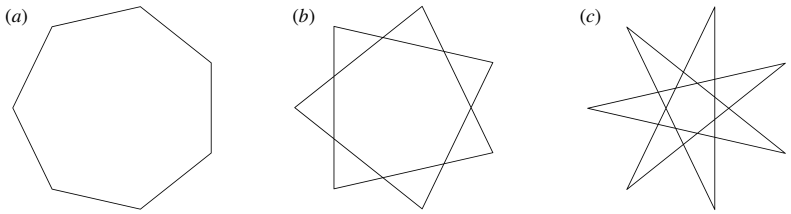

MMR :	8 : 1	9 : 2	10 : 3
Polygon :	{7/1}	{7/2}	{7/3}

Figure A.2: Star polygons corresponding to different 7th order MMRs, illustrating how the period ratio affects the polygon shape even when the resonance order q is fixed. All three MMRs produce cycles with $q = 7$ conjunctions, but differ in their step sizes $d = p - q$, which determines the polygon density. **(a)** 8:1 MMR $\rightarrow$ {7/1} regular heptagon. **(b)** 9:2 MMR $\rightarrow$ {7/2} seven-pointed star. **(c)** 10:3 MMR $\rightarrow$ {7/3} polygon, a denser seven-pointed star.

Appendix B

Approximation for the Effective Perturbing Potential

The full expression for the effective perturbing potential is given by Namouni et al. as a Fourier expansion [14]:

$$W = \frac{1}{2\pi} \sum_{-\infty}^{\infty} W_n \tilde{e}^{in(\lambda-\varpi)} \tag{B.0.1}$$

where λ is the mean longitude of the eccentric outer test particle and ϖ is the longitude of its pericenter. Each coefficient W_n is itself an infinite series in powers of eccentricity:

$$W_n = \sum_{|n|\leq p\leq M} W_n^{p,0} \tilde{e}^p + \ldots \tag{B.0.2}$$

Here, M is the truncation order of the expansion and variables n and p share the same parity. We consider only coplanar systems, so the inclination index $q = 0$[1]. The expansion takes the form:

$$W = W_0 + W_1 + W_2 + W_3 + \ldots \tag{B.0.3}$$

$$= \left(W_0^{0,0} + W_0^{2,0}\tilde{e}^2 + W_0^{4,0}\tilde{e}^4 + \ldots\right) \tag{B.0.4}$$

$$+ \frac{1}{a}\left(W_1^{1,0}\tilde{e} + W_1^{3,0}\tilde{e}^3 + W_1^{5,0}\tilde{e}^5 + \ldots\right)\cos\theta \tag{B.0.5}$$

$$+ \frac{1}{a}\left(W_2^{2,0}\tilde{e}^2 + W_2^{4,0}\tilde{e}^4 + W_2^{6,0}\tilde{e}^6 + \ldots\right)\cos 2\theta \tag{B.0.6}$$

$$+ \frac{1}{a}\left(W_3^{3,0}\tilde{e}^3 + W_3^{5,0}\tilde{e}^5 + W_3^{7,0}\tilde{e}^7 + \ldots\right)\cos 3\theta + \ldots \tag{B.0.7}$$

[1] This simplifies the disturbing function to its planar form, where W_n contains only p-dependent terms.

where we have expressed the real part of the complex exponential in Eq B.0.1 as a cosine.

in the low-eccentricity limit, higher-order terms in $\tilde{e}$ rapidly become negligible. This allows us to approximate each coefficient by its leading-order term:

$$W_n \approx \frac{1}{a} W_n^{n,0}. \tag{B.0.8}$$

This simplification significantly reduces computational complexity by collapsing each Fourier mode to a single term.

To assess the accuracy of this approximation (Eq. B.0.8), we compare the first few terms of the W_n expansion to the function $\mathrm{s}_k(\tilde{e})$ defined in the Celmech package

$$\mathrm{s}_k(\tilde{e}) \approx \frac{(-1)^k \sqrt{3} \exp(k/3)}{\pi k} \tilde{e}^k \tag{B.0.9}$$

which approximates the coefficient of $\cos(k\theta)$ in the Fourier expansion of the potential, as derived by Hadden and Lithwick [6]. In Namouni's notation, these functions are related by:

$$\mathrm{s}_n(\tilde{e}) = W_n / 2\pi. \tag{B.0.10}$$

Figure B.1 plots $\mathrm{s}_1(\tilde{e})$ and $\mathrm{s}_2(\tilde{e})$ for $\tilde{e} = 0$ to 0.7 (solid blue lines). Additionally, we plot the first four terms in the expansions $W_1 = W_1^{1,0}\tilde{e} + W_1^{3,0}\tilde{e}^3 + W_1^{5,0}\tilde{e}^5 + \ldots$ and $W_2 = W_2^{2,0}\tilde{e}^2 + W_2^{4,0}\tilde{e}^4 + W_2^{6,0}\tilde{e}^6 + \ldots$ (dotted lines) along with their partial sums (orange dotted line).

The comparison confirms that higher-order terms rapidly become negligible. This is because all coefficients with $p > 1$ in the expansion of W_1 (Eq. B.0.2) are at least an order of magnitude smaller than the leading term $W_1^{1,0}$, their contributions are further suppressed by increasing powers of the small parameter $\tilde{e}$. Even at $\tilde{e} = 0.7$—well above the values relevant to this study—the leading-order approximation performs remarkably well: the approximation $W_1 \approx W_1^{1,0}$ reproduces $\mathrm{s}_1(\tilde{e})$ to within 7.1% and the approximation $W_2 \approx W_2^{2,0}$ reproduces $\mathrm{s}_2(\tilde{e})$ to within 2.5%.

Since all simulations presented in this work operate at significantly lower eccentricities, we conclude that the use of leading-order approximations for each W_n is well justified.

Finally, we note that the W_n coefficients differ from the constants A_n used throughout this thesis by the relation

$$A_n^2 = \frac{4}{3} \cdot \frac{|W_n|}{2\pi}. \tag{B.0.11}$$

We adopt the A_n notation because it simplifies numerical factors in later expressions, as formulated by Tamayo and Hadden (2025) [18].

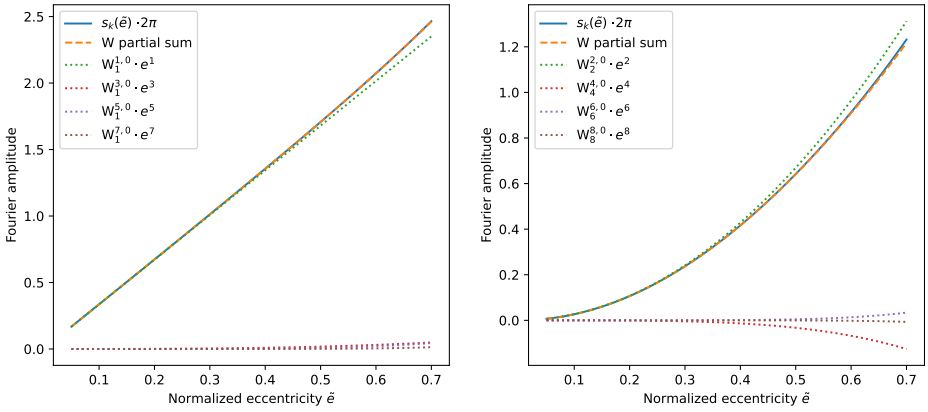

Figure B.1: Comparison between the Fourier coefficients of the effective potential computed via the Celmech function $s_k(\tilde{e})$ (solid blue lines) and the truncated eccentricity expansions of the corresponding W_n terms from Namouni's formalism [14]. **Left:** The coefficient of $\cos(\theta)$ (i.e., $n = 1$) is plotted as a function of normalized eccentricity $\tilde{e}$. The leading-order term $W_1^{1,0}\tilde{e}$ dominates, with higher-order terms $W_1^{3,0}\tilde{e}^3$, $W_1^{5,0}\tilde{e}^5$, and $W_1^{7,0}\tilde{e}^7$ contributing minimally. Their partial sum (dashed orange) closely tracks $s_1(\tilde{e})$. **Right:** Same comparison for $n = 2$, corresponding to $\cos(2\theta)$. Again, the leading term $W_2^{2,0}\tilde{e}^2$ dominates, with higher-order corrections providing only small deviations. Even at $\tilde{e} = 0.7$, the leading-order approximations remain accurate to within a few percent, justifying their use throughout this work.

Appendix C

A Discrete Mapping Model for the PCRBP in the Hill Limit

As discussed in Sec 2.3, the assumption of low eccentricity and closely spaced orbits allows for a simplified treatment of the planar circular restricted three-body problem (PCR3BP), where the dynamics can be approximated as a discrete map: the orbits evolve as unperturbed Keplerian ellipses between conjunctions, with impulsive gravitational kicks applied at each close approach. This technique, which maps the change in orbital elements from one conjunction to the next, has been developed in several prior studies including Duncan et al 1989 and Namouni et al 1996 [3, 14]. The analysis by Duncan et al. (hereafter called DQT) treats the case of initially circular, coplanar orbits and derives a first-order approximation of the mapping. Namouni considers the more general case of two massive, eccentric planets in the Hill Limit and extends the mapping to higher orders. In this thesis, we follow the frameworks developed by these papers to derive an expression for the test particle's fractional kick to mean motion at each conjunction.

Equation 4.1.2 in the main text gives the total change in mean motion as an infinite series in e. In this appendix, we derive that result. We begin by using the first-order map from DQT to verify the corresponding first-order mapping in Namouni's analysis. We then apply this framework to recover the second-order mapping presented by Namouni, correcting a few typographical errors and reformulating parts of the mapping to make it easier to generalize. Finally, we extend the analysis to arbitrary order, deriving a general expression for the discrete kick to mean motion as an infinite series in powers of e.

C.1 First Order Mapping between Conjunctions

The analysis by DQT studies the planar circular three body problem (PCRBP) described in Sec 2.1. In their framework, the eccentricity vector z is defined as

$$z = e\exp\{(i\varpi_D)\}, \tag{C.1.1}$$

where e is the eccentricity of the test particle's orbit and ϖ_D is the longitude at which the two orbits are maximally separated.

Some authors (e.g., Namouni 1996, Murray & Dermott 1999) instead define the conjunction angle θ' as measured from the point of minimum separation, such that $\theta = \phi + \pi$ [13, 14]. This convention places the equilibrium point of the MMR at $\phi = 0$, in analogy with the usual pendulum potential. However, as discussed in Sec. 6 of Tamayo and Hadden 2025, this choice introduces undesirable features for higher-order resonances [18]. We therefore retain the definition of θ used by DQT, which places the equilibrium at $\theta = \pi$.

To distinguish between mappings from different sources throughout this appendix, we label variables from DQT with the subscript D and variables from Namouni with the subscript N, as needed.

The relative semimajor axis is defined as

$$\varepsilon = \frac{a - a_p}{a_p} \tag{C.1.2}$$

where a is the semimajor axis of the eccentric test particle and a_p is the semimajor axis of the planet on the circular orbit. For an outer test particle, $\varepsilon > 0$, while for an inner test particle $\varepsilon < 0$. The mean longitude of the test particle is denoted by λ.

Using linear perturbation theory methods (as outlined by e.g. Julian and Toomre 1966 and Henon and Petit 1986), DQT derives expressions for the discrete changes in z, ϖ, and λ to first order [7, 10]. As given in Eq. 17 of their paper, this first order mapping is:

$$z_{n+1} = z_n + g\mu\frac{i\exp\{(i\lambda_n)\}}{\varepsilon_1^2}\mathrm{sgn}(\varepsilon_1) \tag{C.1.3}$$

$$\Delta\varepsilon_{n+1} = \frac{2(|z_{n+1}|^2 - |z_n|^2)}{3\varepsilon_1} \tag{C.1.4}$$

$$\lambda_{n+1} = \lambda_n + \frac{4\pi}{3\varepsilon_1} - \frac{4\pi\Delta\varepsilon_{n+1}}{3\varepsilon_1^2} \tag{C.1.5}$$

where $g = \frac{8}{9}[2K_0(2/3) + K_1(2/3)] = 2.23956667$ and $\mu = m/M$ is the reduced mass of the system.

Namouni derives a similar mapping using Hamiltonian perturbation theory in the Hill limit. In this formulation, the disturbing function is expressed as a potential W expanded in powers of eccentricity and Fourier modes of the resonant

angle (see Appendix B). To second order, the potential is given by:

$$W = 2W_1^{1,0}\frac{\sqrt{2I}}{a_1^2}\cos(\phi-\lambda) \tag{C.1.6}$$

$$+ (W_0^{2,0} + 2W_2^{2,0}\cos(2(\phi-\lambda)))\frac{2I}{a_1^3}. \tag{C.1.7}$$

where I is the canonical action variable (proportional to e^2) and a_1 is the semimajor axis scaled to the planet's orbit.

To obtain a discrete mapping, changes in I and ϕ are computed from the derivatives of W

$$\Delta I = -\frac{\partial W}{\partial \phi}, \quad \Delta\phi = \frac{\partial W}{\partial I}. \tag{C.1.8}$$

(See Eqs. 24–29 in Namouni et al. 1996 for the full derivation).

Because ϕ becomes undefined in the circular limit $I \to 0$, Namouni separates the potential into a singular part W_{sing}, which contains the first order term, and the remaining W containing all higher order terms. The first-order mapping is then obtained using W_{sing} in Cartesian coordinates, where the singularity is avoided. Higher order corrections are subsequently calculated as perturbations on top of this first order solution.

Recovering Namouni's First-Order Mapping from DQT

DQT and Namouni approach the mapping problem using different variables, conventions, and coordinate choices. In this section, we reconcile these differences and show explicitly that the first-order mapping presented by Namouni can be derived from the mapping developed by Duncan et al.

We begin by considering the first order mapping in Duncan, given by Eq. C.1.3 - C.1.5. Our analysis in the main body focuses on the an outer test particle. Although the final result is valid for both inner and outer particles, the sign of ε depends on the orbital configuration. To match our setup, we proceed assuming an outer test particle.

For this case, we define

$$\varepsilon = a_{12}\epsilon \tag{C.1.9}$$

where $a_{12} = (a - a_p)/\epsilon a_p$ is the relative semimajor axis in Hill units, normalized by the planet's semimajor axis a_p, and ϵ is the small mass parameter $\epsilon = \left(\frac{\mu}{3}\right)^{1/3}$. The initial value of this parameter is $a_{12,0}$.

To convert DQT's expressions to Namouni's conventions, we decompose the complex eccentricity z into real and imaginary vector components

$$h_D = e\cos\varpi_D, \qquad k_D = e\sin\varpi_D. \tag{C.1.10}$$

Noting that $\text{sgn}(\varepsilon_1) > 0$, we use Eq C.1.3 - C.1.5 to derive a mapping for these variables:

$$h_{D,n+1} = h_{D,n} - \frac{g\mu}{a_{12,0}^2 \epsilon^2} \sin(\lambda_n) = h_{D,n} - \frac{2W_1^{1,0}\epsilon}{a_{12,0}^2} \sin(\lambda_n) \tag{C.1.11}$$

$$k_{D,n+1} = k_{D,n} + \frac{g\mu}{a_{12,0}^2 \epsilon^2} \cos(\lambda_n) = k_{D,n} + \frac{2W_1^{1,0}\epsilon}{a_{12,0}^2} \cos(\lambda_n). \tag{C.1.12}$$

In the second equality of each expression, we have used $\mu = 3\epsilon^3$ and the parameter $g = \frac{2}{3} W_1^{1,0}$, where the constant $W_1^{1,0}$ is defined in Appendix B of Namouni.

In addition to using a different angle $\phi = \pi + \varpi_D$ from DQT, Namouni also defines the relative semimajor axis variable a_r in the opposite direction to DQT's a_{12}. Since a_r is negative for an outer test particle, we retain a_{12} for this derivation to avoid sign complications.

In Namouni's variables, the eccentricity vector components are:

$$h_N = e\cos\phi/\epsilon, \quad k_N = e\sin\phi/\epsilon. \tag{C.1.13}$$

Because $\phi = \pi + \varpi_D$, we have:

$$h_D = -\epsilon h_N, \quad k_D = -\epsilon k_D \tag{C.1.14}$$

Substituting these expressions into Eq. C.1.11 and C.1.12, we obtain the mapping in Namouni's variables:

$$h_{N,n+1} = h_{N,n} + \frac{2W_1^{1,0}}{a_{12,0}^2} \sin(\lambda_n) \tag{C.1.15}$$

$$k_{N,n+1} = k_{N,n} - \frac{2W_1^{1,0}}{a_{12,0}^2} \cos(\lambda_n) \tag{C.1.16}$$

From the mapping for complex eccentricity in Eq. C.1.3 , the pericenter angle ϖ_D at time step $n+1$ is:

$$\varpi_{D,n+1} = \arctan\left(\frac{k_{D,n+1}}{h_{D,n+1}}\right) \tag{C.1.17}$$

Therefore, the angle ϕ used in Namouni at time step $n+1$ becomes:

$$\phi_{n+1} = \varpi_{D,n+1} + \pi = \arctan\left(\frac{k_{D,n+1}}{h_{D,n+1}}\right) + \pi \tag{C.1.18}$$

$$= \arctan\left(\frac{-k_{N,n+1}}{-h_{N,n+1}}\right) + \pi \tag{C.1.19}$$

$$= \arctan\left(\frac{k_{N,n+1}}{h_{N,n+1}}\right). \tag{C.1.20}$$

Namouni also defines the canonical action angle $I = \frac{e^2}{2}$ related to the eccentricity e expressed in Hill's units. The mapping for this variable from one conjunction to the next can be written in terms of Cartesian h_N and k_N as follows:

$$I_{n+1} = \frac{1}{2}(h^2_{N,n+1} + k^2_{N,n+1}) \tag{C.1.21}$$

This result matches Eq. 39 in Namouni 1996.

To track changes in the semimajor axis between conjunctions, Namouni uses the variable

$$K = 3a^2_{12}/8 = 3a^2_r/8 \tag{C.1.22}$$

where $a^2_{12} = a^2_r$ as the two variables differ only by a sign.

We are now in a position to develop the first order mapping used by Namouni from DQT's mapping (Eq. C.1.3 - C.1.5).

Starting from Eq. C.1.5, we write:

$$\varepsilon\Delta\varepsilon = \frac{2}{3}(|z_{n+1}|^2 - |z_n|^2) \tag{C.1.23}$$

$$= \frac{4\epsilon^2}{3}[I_{n+1} - I_n]. \tag{C.1.24}$$

Substituting $\varepsilon = a_{12}\epsilon$ yields:

$$a_{12}\Delta a_{12} = \frac{4}{3}\Delta I \tag{C.1.25}$$

From Eq. C.1.22 for K, it follows that

$$\Delta K = \frac{3}{4}a_{12}\Delta a_{12} \tag{C.1.26}$$

From this, we recover the relationship in Eq. 34 of [14]:

$$\Delta K = \Delta I \tag{C.1.27}$$

Finally, we express λ_{n+1} in Namouni's variables. Starting from Eq. C.1.5,

$$\lambda_{n+1} = \lambda_n + \frac{4\pi}{3\varepsilon_1} - \frac{4\pi\Delta\varepsilon_{n+1}}{3\varepsilon_1^2} \tag{C.1.28}$$

$$= \lambda_n + \frac{4\pi}{3\varepsilon_1}\left(1 - \frac{\Delta\varepsilon}{\varepsilon_1}\right) \tag{C.1.29}$$

$$\approx \lambda_n + \frac{4\pi}{3\varepsilon_1}\left(1 + 2\frac{\Delta\varepsilon}{\varepsilon_1}\right)^{-1/2} \tag{C.1.30}$$

$$= \lambda_n + \frac{4\pi}{3\epsilon}\frac{1}{\sqrt{\frac{\varepsilon_1^2}{\epsilon^2} + 2\frac{\varepsilon_1\Delta\varepsilon}{\epsilon^2}}} \tag{C.1.31}$$

where in the third line we have used the binomial approximation assuming the inner planet has a small enough mass and the planes are sufficiently separated so that changes to the semimajor axis $\Delta\varepsilon/\varepsilon_1$ are small.

Using Eq. C.1.9 and C.1.22, we see that $K_n = \frac{3}{8}\frac{\varepsilon^2}{\epsilon^2}$ and $\Delta K_n = \frac{3}{4}\frac{\varepsilon_1 \Delta\varepsilon}{\epsilon^2}$. Substituting, we obtain:

$$\lambda_{n+1} = \lambda_n + \frac{4\pi}{3\epsilon}\frac{1}{\sqrt{\frac{8}{3}(K_n + \Delta K)}} \tag{C.1.32}$$

$$= \lambda_n + \frac{4\pi}{3\epsilon}\frac{1}{\sqrt{8K_{n+1}/3}} \tag{C.1.33}$$

which matches Eq. 43 from Namouni.

Summary of First Order Mapping

We have shown that the mapping for eccentricity, semimajor axis, and mean longitude from DQT is consistent with the first-order mapping presented by Namouni. Summarizing Namouni's first-order mapping, the evolution of the orbital elements from one conjunction to the next is given by:

$$h_n = \sqrt{2I_n}\cos\varpi \tag{C.1.34}$$

$$k_n = \sqrt{2I_n}\sin\varpi \tag{C.1.35}$$

$$h_{n+1} = h_n + \frac{2W_1^{1,0}}{a_r^2}\sin\lambda_n \tag{C.1.36}$$

$$k_{n+1} = k_n - \frac{2W_1^{1,0}}{a_r^2}\cos\lambda_n \tag{C.1.37}$$

$$I_{n+1} = \frac{1}{2}(h_{n+1}^2 + k_{n+1}^2) \tag{C.1.38}$$

$$\varpi_{n+1} = \arctan(k_{n+1}/h_{n+1}) \tag{C.1.39}$$

$$K_{n+1} = K_n + I_{n+1} - I_n \tag{C.1.40}$$

$$\lambda_{n+1} = \lambda_n + \frac{4\pi}{3\epsilon\sqrt{8K_{n+1}/3}} \tag{C.1.41}$$

These expressions form the foundation for the discrete kick model used throughout this thesis. They define the evolution of a particle's orbital parameters due to a single conjunction and provide the basis for extensions to higher-order mappings.

C.2 Higher Order Discrete Mappings

Namouni calculates higher order terms in the mapping by first evaluating the first order evolution using the singular part of the potential, W_{sing} which re-

mains finite as $I \to 0$. As discussed earlier, this step allows the mapping to be constructed even for nearly circular orbits. The resulting "primed" variables (h', k', I', ϕ') are then used to evaluate higher-order corrections to the action and angle variables. Following this method, the second-order mapping can be written as:

$$h_n = \sqrt{2I_n}\cos\varpi \tag{C.2.1}$$

$$k_n = \sqrt{2I_n}\sin\varpi \tag{C.2.2}$$

$$h' = h_n + \frac{2W_1^{1,0}}{a_r^2}\sin\lambda_n \tag{C.2.3}$$

$$k' = k_n - \frac{2W_1^{1,0}}{a_r^2}\cos\lambda_n \tag{C.2.4}$$

$$I' = \frac{1}{2}(h'^2 + k'^2) \tag{C.2.5}$$

$$\varpi' = \arctan(k'/h') \tag{C.2.6}$$

$$I_{n+1} = I' - 4W_2^{2,0}\sin(2(\phi' - \lambda_n))2I_{n+1}/a_r^3 \tag{C.2.7}$$

$$\phi_{n+1} = \phi_n - (W_0^{2,0} + 2W_2^{2,0}\cos(2(\phi' - \lambda_n)))\frac{2}{a_r^3} \tag{C.2.8}$$

$$K_{n+1} = K_n + I_{n+1} - I_n \tag{C.2.9}$$

$$\lambda_{n+1} = \lambda_n + \frac{4\pi}{3\epsilon\sqrt{8K_{n+1}/3}} \tag{C.2.10}$$

Differences from Namouni's Presentation

Our version of this mapping contains several differences from Eq. 36-43 in the Namouni paper:

- Eq. C.2.3 uses $\sin\lambda_n$ whereas the corresponding Eq. 37 from Namouni uses $\cos\lambda_n$
- Eq. C.2.4 uses $\cos\lambda_n$ whereas the corresponding Eq. 38 from Namouni uses $\sin\lambda_n$
- The angle in Eq. C.2.7 (and Eq. C.2.8) is $\phi' - \lambda$ whereas Namouni Eq. 40 (and 41) uses $\lambda - \phi'$.

To develop even higher orders of this mapping, one simply uses higher orders of the initial potential function W.

We have verified the first two corrections by matching with the first order mapping from Duncan et. al. The third correction is confirmed by comparing phase-space trajectories of this mapping against numerical integrations.

Reformulation in Unscaled Units

Namouni's mapping is formulated in Hill units and defines the angle ϕ as shifted by π from the reference angle used by DQT. For consistency with our analysis, we reformulate Namouni's mapping without Hill scaling units and adopt DQT;s reference angle convention (recall that the new definition of ϖ ensures the reference angle does not jump by π for higher order terms, which is important for our result which includes to higher order terms). We also note that

$$\sqrt{2I_n}/a_1 = \tilde{e} = e/e_c, \tag{C.2.11}$$

where e_c is the crossing eccentricity. This substitution allows us to express the mapping directly in terms of $\tilde{e}$, simplifying the expansion of the potential and the resulting evolution equations.

The potential function to second order using these conventions is:

$$W = 2W_1^{1,0}\cos(\lambda-\varpi)\epsilon\frac{\tilde{e}}{e_c} \tag{C.2.12}$$

$$+ (W_0^{2,0} + 2W_2^{2,0}\cos(2(\lambda-\varpi)))\epsilon\frac{\tilde{e}^2}{e_c}. \tag{C.2.13}$$

Using the identity in Eq. C.2.11 and converting all variables from Hill units, the second-order mapping becomes:

$$\tilde{h}_n = \tilde{e}_n\cos\varpi \tag{C.2.14}$$

$$\tilde{k}_n = \tilde{e}_n\sin\varpi \tag{C.2.15}$$

$$\tilde{h}'_n = \tilde{h}_n - \frac{2W_1^{1,0}\mu}{3e_c^2}\sin\lambda_n \tag{C.2.16}$$

$$\tilde{k}'_n = \tilde{k}_n + \frac{2W_1^{1,0}\mu}{3e_c^2}\cos\lambda_n \tag{C.2.17}$$

$$(\tilde{e}')^2 = (\tilde{h}'_n)^2 + (\tilde{k}'_n)^2 \tag{C.2.18}$$

$$= (\tilde{e}_n)^2 - \tilde{e}_n\frac{4\mu W_1^{1,0}}{3e_c^3}\sin(\lambda_n-\varpi_n) + \left(\frac{2\mu W_1^{1,0}}{3e_c^3}\right)^2 \tag{C.2.19}$$

$$\varpi' = \arctan(\tilde{k}'/\tilde{h}') \tag{C.2.20}$$

$$(\tilde{e}_{n+1})^2 = (\tilde{e}')^2 - 4W_2^{2,0}\sin(2(\lambda_n-\varpi'))\frac{\epsilon}{e_c^3}\tilde{e}_{n+1}^q \tag{C.2.21}$$

$$\frac{a_{n+1}}{a_0} = \frac{a_n}{a_0} + \frac{2e_c}{3}((\tilde{e}_{n+1})^2 - (\tilde{e}_n)^2) \tag{C.2.22}$$

$$\varpi_{n+1} = \varpi' - (W_0^{2,0} + 2W_2^{2,0}\cos(2(\varpi'-\lambda_n)))\frac{2\mu}{e_c^3} \tag{C.2.23}$$

$$\lambda_{n+1} = \lambda_n + \frac{4\pi}{3a_{n+1}/a_0} \tag{C.2.24}$$

C.3 Analytical Expression for the Kick to Mean Motion

For the analysis presented in the main body of this thesis, we are interested in determining the discrete change in mean motion that occurs at each conjunction. Through Kepler's third law, changes to mean motion n and semimajor axis a are related by:

$$\frac{\delta n}{n} = -\frac{3}{2}\frac{\delta a}{a} \tag{C.3.1}$$

where $\delta n = n_{n+1} - n_n$ and $\delta a = a_{n+1} - a_n$.

From the second order mapping in Eq. C.2.22, we find the kick to semimajor axis can be written as

$$\frac{\delta a_r}{a_0} = -\frac{8}{9}\frac{e\mu}{e_c^3} W_1^{1,0} \sin\theta \tag{C.3.2}$$

where we have used $\mu = 3\epsilon^3$. Substituting this into Eq C.3.1 and using the approximation $W_1^{1,0} \approx W_1$ where $A_n^2 = \frac{4}{3}\frac{|W_n|}{2\pi}$ (see Appendix B) yields the second order kick to mean motion:

$$\frac{\delta n}{n} \approx 2\pi \frac{\mu}{e_c^2} A_1 \tilde{e} \sin\theta \tag{C.3.3}$$

This leading order term arises from the first Fourier mode of the disturbing potential W. Extrapolating from this and higher order terms, we find that the total kick to mean motion takes the form of an infinite Fourier series:

$$\frac{\delta n}{n} \approx 2\pi \frac{\mu}{e_c^2} \sum_{j=1}^{\infty} j A_j^2 \tilde{e}^j \sin(j\theta), \tag{C.3.4}$$

We confirm this expression numerically in Fig 4.1, which shows excellent agreement between the numerically computed kick strength and the analytical Fourier series as a function of the conjunction angle θ.

Bibliography

[1] William F Bottke, David Vokrouhlickỳ, and David Nesvornỳ, *An asteroid breakup 160 myr ago as the probable source of the k/t impactor*, Nature **449** (2007), no. 7158, 48–53.

[2] Alan Chamberlain, *Kirkwood gaps asteroid distribution plot*, https://ssd.jpl.nasa.gov/diagrams/mb_hist.html, 2006, Plot by Alan Chamberlain (JPL/Caltech), via Wikimedia Commons. Accessed: 2025-05-02.

[3] Martin Duncan, Thomas Quinn, and Scott Tremaine, *The long-term evolution of orbits in the solar system: A mapping approach*, Icarus **82** (1989), no. 2, 402–418.

[4] P. Goldreich and S. Tremaine, *Disk-satellite interactions*, Astrophysical Journal **241** (1980), 425–441.

[5] Sam Hadden, *An Integrable Model for the Dynamics of Planetary Mean-motion Resonances*, Astronomical Journal **158** (2019), no. 6, 238.

[6] Sam Hadden and Yoram Lithwick, *A criterion for the onset of chaos in systems of two eccentric planets*, The Astronomical Journal **156** (2018), no. 3, 95.

[7] Michel Hénon and Jean-Marc Petit, *Series expansions for encounter-type solutions of hill's problem*, Celestial Mechanics **38** (1986), no. 1, 67–100.

[8] Jacques Henrard, Anne Lemaitre, Andrea Milani, and CD Murray, *The reducing transformation and apocentric librators*, Celestial mechanics **38** (1986), no. 4, 335–344.

[9] George William Hill, *Researches in the lunar theory*, American journal of Mathematics **1** (1878), no. 1, 5–26.

[10] W. H. Julian and A. Toomre, *Non-Axisymmetric Responses of Differentially Rotating Disks of Stars*, Astrophysical Journal **146** (1966), 810–+.

[11] Allan J Lichtenberg and Michael A Lieberman, *Regular and stochastic motion*, vol. 38, Springer Science & Business Media, 2013.

[12] Renu Malhotra, Matthew Holman, and Takashi Ito, *Chaos and stability of the solar system*, Proceedings of the National Academy of Sciences **98** (2001), no. 22, 12342–12343.

[13] C. D. Murray and S. F. Dermott, *Solar System Dynamics*, Cambridge U. Press, Cambridge, 1999.

[14] F. Namouni, J. F. Luciani, S. Tabachnik, and R. Pellat, *A mapping approach to Hill's distant encounters: application to the stability of planetary embryos.*, Astronomy & Astrophysics **313** (1996), 979–992.

[15] SJ Peale, *Orbital resonances in the solar system*, Annual review of astronomy and astrophysics **14** (1976), no. 1, 215–246.

[16] Antoine C Petit, *An integrable model for first-order three-planet mean motion resonances*, Celestial Mechanics and Dynamical Astronomy **133** (2021), no. 8, 39.

[17] Antoine C Petit, Gabriele Pichierri, Melvyn B Davies, and Anders Johansen, *The path to instability in compact multi-planetary systems*, Astronomy & Astrophysics **641** (2020), A176.

[18] Daniel Tamayo and Samuel Hadden, *A unified, physical framework for mean motion resonances*, arXiv preprint arXiv:2410.21748 (2024).

[19] Scott Tremaine, *Dynamics of planetary systems*, vol. 63, Princeton University Press, 2023.

[20] Manuel Vogel, *An introduction to the theory of numbers, 6th edition, by g.h. hardy and e.m. wright*, Contemporary Physics - CONTEMP PHYS **51** (2010), 283–283.

[21] Eric W. Weisstein, *Star polygon*, Accessed on 2025-05-01.

[22] J. Wisdom, *A perturbative treatment of motion near the 3/1 commensurability*, **63** (1985), no. 2, 272–289.